Integrated topological optimization and production of an additively manufactured steel T-joint

A case study

Monteiro, Kaike; Zhu, Carlos; Santos, Ana Francisca; da Silva, Luís Simões; Tankova, Trayana

DOI
10.1016/j.istruc.2025.108511

Publication date
2025

Document Version
Final published version

Published in
Structures

Citation (APA)
Monteiro, K., Zhu, C., Santos, A. F., da Silva, L. S., & Tankova, T. (2025). Integrated topological optimization and production of an additively manufactured steel T-joint: A case study. *Structures*, *74*, Article 108511. https://doi.org/10.1016/j.istruc.2025.108511

Structures 74 (2025) 108511

Contents lists available at ScienceDirect

Structures

journal homepage: www.elsevier.com/locate/structures

Integrated topological optimization and production of an additively manufactured steel T-joint: A case study

Kaike Monteiro [a,*], Carlos Zhu [a,b], Ana Francisca Santos [a], Luís Simões da Silva [a], Trayana Tankova [c]

[a] University of Coimbra, ISISE, ARISE, Department of Civil Engineering, Coimbra, Portugal
[b] University of Coimbra, CEEMPRE, ARISE, Department of Mechanical Engineering, Coimbra, Portugal
[c] Technische Universiteit Delft, Department of Engineering Structures, Delft, Netherlands

ARTICLE INFO

Keywords:
Steel
WAAM
Additive manufacturing
Joints
Topology optimization

ABSTRACT

Additive manufacturing (AM) rapidly expands to all research areas due to its multiple advantages, such as the freedom and flexibility in achieving any geometry. Using AM as a fabrication technique, the design process has almost no limitations, blending considerably well with the irregular geometries that may result from topology optimization. Yet, in practice the application of AM together with topologically optimized geometries is not as straightforward. In this research, a hollow square t-joint is used as a case study to investigate and understand the difficulties in the design and manufacturing of steel parts using wire arc additive manufacturing (WAAM). The case study showcases from the application of two optimization methods with various parameters to find an optimal geometry; numerical analysis (FEM) on non-optimized and optimized models; a procedure called "re-engineering" that adjusts the optimized geometry to structure efficiency and AM effectiveness; dynamic slicing and path planning; an adjustment of the welding parameters to enhance the material properties and accuracy of the final specimens; and experimental assessments on non-optimized and optimized printed t-joints to validate the entire process. The application of this process allowed the manufacture of a complex optimized geometry, which have more resistance than the non-optimized T-joint.

1. Introduction

Automation in construction is an essential feature [1], which relates efficient use of resources in design, fabrication and assembly. In construction, the design phase of a structure represents 5 % of the whole structure development but may impact 75 % of the overall costs [2]. Therefore, incorporating optimization strategies and automation techniques in structural design is crucial in view of sustainability. Wire arc additive manufacturing (WAAM) is an emerging technology which is automatic, and it can deposit material in an optimum way, only where it is needed. Topology optimization (TO) is a sustainable and cost-efficient design process due to the ability to obtain an optimal structure configuration by efficient material distribution [3].

It is widely used in many sectors; however, taking advantage of its full potential is challenging due to the irregularities of the final geometry, which may be complex and costly to manufacture. Until recently, TO was applied together with machining or preparation of moulds for metal casting [4,5]. Nowadays, Additive Manufacturing opens new possibilities for TO where the restrictions in machining and metal casting are no longer problematic [6]. Yet, the optimized geometry resulting from TO software is usually not directly suitable for fabrication because of irregularities after many cycles of removing and adding material at different locations, curves, small angles, and limited thickness, which can be challenging for some additive manufacturing processes. On the other hand, the manufacturing process parameters, such as speed, welding parameters and sequence, influence the geometry of the build. Hence, fabrication can benefit from a geometry which already considers the process limitations. An ideal workflow using WAAM consists of a CAD model which is used to create the *Slicing* and then tool path planning and production (see Fig. 1). The irregular geometry enforces the use of different production parameters in distinct areas of the part which can result in iterations between the initial *CAD model*, *Slicing* and *Production planning*. Additionally, if the fabrication restrictions are considered in TO, the workflow becomes even more complex involving iterations in every step and is time consuming. All these together make it inapplicable to an industrial setup (see Fig. 2).

The objective of this research is to explore how TO and AM can be

* Correspondence to: Department of Civil Engineering, University of Coimbra, Polo II, Rua Luís Reis Santos, Coimbra 3030-788, Portugal.
E-mail address: kpm@uc.pt (K. Monteiro).

https://doi.org/10.1016/j.istruc.2025.108511
Received 7 June 2024; Received in revised form 21 January 2025; Accepted 14 February 2025
Available online 1 March 2025

Acronyms

AM	Additive Manufacturing
FEM	Finite Element Method
WAAM	Wire-Arc Additive Manufacturing
TO	Topology Optimization
CAD	Computer-Aided Design
ESO	Evolutionary Structural Optimization
BESO	Binary Evolutionary Structural Optimization
SIMP	Solid isotropic material with penalization
RAMP	Rational Approximation of Material Properties
DMLS	Direct Metal Laser Sintering
DED	Direct Energy Deposition
CMT	Cold Metal Transfer
DIC	Digital Image Correction
DB1	Design Block 1
DB2	Design Block 2
DEF	Abaqus Default
CB	Condition-Based Algorithm

Fig. 1. Linear (ideal) workflow.

applied together to integrate the design and fabrication stages. Hence, a hollow section T-joint is chosen being a simple and known geometry in terms of stresses, and failure modes. The experimental tests and numerical simulations would not introduce additional uncertainties, allowing to focus on the assessment of the optimization process, where the optimum stress and material distribution is straightforward to determine when loaded in tension, and the validation of the entire process would be feasible by an optimized version of the T-Joint. This case study is used to address various TO processes and discusses which are the most suitable design constraints. It also examines the fabrication challenges and provides possible strategies on how to solve them. Finally, it validates experimentally the conclusions based on numerical simulations.

In this paper, firstly a brief literature review on topology optimization and additive manufacturing is proposed, aiming to facilitate the understanding of the analysis of results. Then, the adopted methodology is presented, followed by experimental and numerical analyses of the proposed case study. Finally, recommendations are given for the design and manufacturing of steel parts using WAAM in combination with TO.

2. Literature review

2.1. Topology optimization of joints

Structural optimization is the process of assembling materials or structural elements in the best way possible to maximize structural efficiency. It is extensively used due to its beneficial impact on cost and it is commonly combined with a computer-based method like the Finite Element Method (FEM) [7]. What defines the "best structure" depends on the optimization goal. For structural optimization, this is the objective function, which is a mathematical expression that can be maximized or minimized to quantify a structure's performance [8]. These functions represent a quantifiable unit, such as the members' weight, the structure's stiffness, the overall cost, the sensitivity to a specific failure mode such as buckling, etc. Therefore, it is critical to determine the mathematical model's variables, such as the number of variables that define the size of the mathematical model, the number of possible solutions, and, consequently, the computational cost required for the analysis [7].

Another significant factor in optimization is the application of constraints. Although not a requirement, these constraints can be crucial to

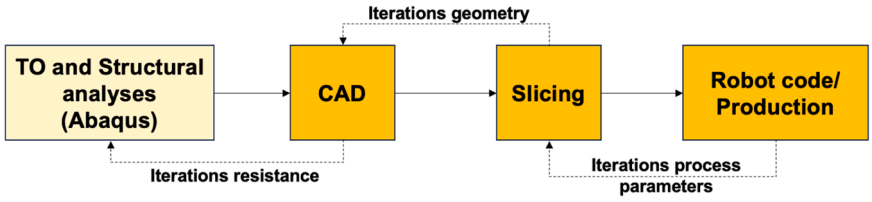

Fig. 2. Iterative (real) workflow.

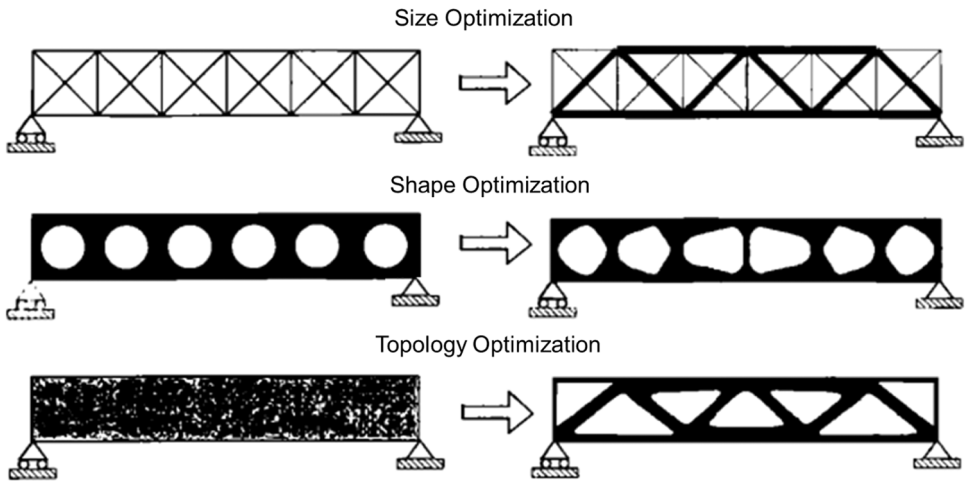

Fig. 3. Types of Structure Optimization [10].

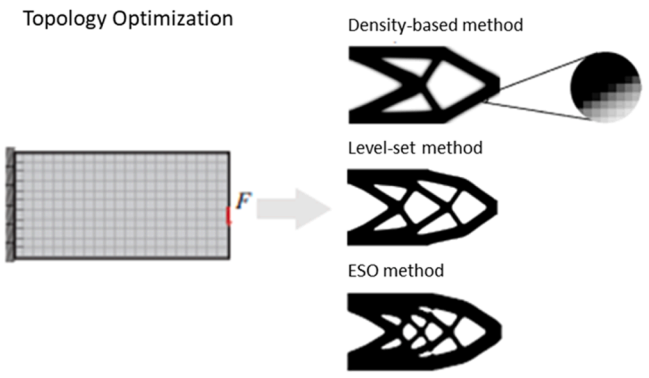

Fig. 4. Types of topology optimization [20].

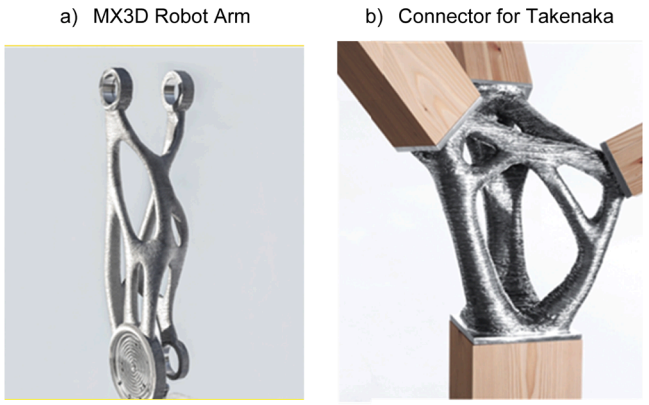

Fig. 5. Example of TO Structures manufactured with WAAM, a) MX3D Robot Arm [25], b) Connector for Takenaka [26].

the search domain, the computational cost, and the effectiveness of the process. The constraints are pre-selected values that remain constant during the optimization procedure and restrain the search domain (i.e., the volume, cross-section, stresses, etc. [7]).

Structural optimization can be divided into Size, Shape, and Topology Optimization (see Fig. 3). The first is the remodelling of the structure's size and boundaries, for instance, attempting to find the optimal cross-section or thickness. Secondly, Shape Optimization tries to adjust the shape of the structure, varying the material position within the same volume. Lastly, Topology Optimization (TO) is the most used among the optimization procedures since it integrates the other two to have the capability to vary size and shape in the design domain creating a different structure [9].

Unlike shape optimization, TO can remove and add any quantity of material in all directions, even around the boundaries when not constrained. Moreover, TO is mainly used because the process does not require any restraints, including when there are holes, gaps, or an irregular geometry. Therefore, it can modify the material or void position or fill and create openings in other areas in the same process, indicating the method's effectiveness and adaptability [10,11].

TO may be categorized but not exclusive into level-set, evolutionary structural optimization, and density-based methods. The level-set method [12–14] uses an explicit mathematical expression to represent the structural boundary between solids and voids and evaluates the sensitivity of material removal from the design domain. Evolutionary Structural Optimization (ESO) methods [15,16] and Binary Evolutionary Structural Optimization (BESO), introduced first by Xie and Steven in 1997 [15,17], consist on the progressive and slow removal and addition of material that is not useful for the overall structure's performance, for instance, in unstressed parts.

Lastly, in the density-based method [10,18,19], introduced by Bendsoe and Sigmund [18], optimization is performed regarding the characteristics of elements and nodes. In contrast to the other methods, there are a range of elements that are not eliminated nor are fully dense, called intermediate elements (see Fig. 4). This method may be further divided into sensitivity-based and condition-based approaches. In the first, the density of the elements can assume values between 0 and 1 in the final optimized shape. Therefore, the elements can be fully dense (close to 1), have almost no density (close to 0), or have intermediate density. One of the topology optimization approaches applied today is the Solid Isotropic Material with Penalization (SIMP), which is a sensitivity-based approach. Still, the intermediate elements are penalized, resulting in a more smooth algorithm. In contrast, in the condition-based approach, the element's density can assume values between 0 and 1 mainly and intermediate elements rapidly tend to the extremes, converging in fewer optimization cycles to a final geometry with almost no intermediate elements.

Nowadays, some structural analysis software, such as ABAQUS [21], already incorporate topology optimization methods, which increases their suitability for practical use, particularly for specific components such as joints.

Topology optimization applied to structural joints is a relatively new topic; consequently, most research occurred in recent years [3,19,22–26]. This field of study may not have been discussed earlier because there were many limitations regarding the fabrication of the optimized and irregular joints. However, introducing new fabrication processes such as Additive Manufacturing (AM) can eliminate or minimize these limitations and provide an effective way to produce them. Fig. 5 shows some examples of AM optimized joints.

2.2. *Additive manufacturing of TO parts*

The manufacturing method can further restrict the use of an optimized component since the achieved model must be feasible to manufacture (manufacturability) [27]. This issue can lead to a complete redesign, often reducing the targeted performance [28]. For this reason, the research and development of Topology Optimization (TO) has shifted from traditional manufacturing methods, such as machining, injection moulding, and casting, towards additive manufacturing methods [29,30]. AM is considered a less restrictive method that allows the fabrication of more complex TO models, as demonstrated by Arup [31] in the redesign of an existing structural node manufactured using Direct Metal Laser Sintering (DMLS). Also, using DMLS, an optimized component for an Airbus A350 XWB was manufactured, achieving close to a 30 % weight reduction [32]. To bridge this gap, there has been a focused effort to research the integration of AM design constraints into the topology optimization process [3]. This link is discussed in [30] and [3] when documenting the current trends and challenges for AM integrated with TO.

Nowadays, most research focuses on combining topology optimization with the Powder Bed Fusion, particularly DMLS, due to the ability to produce highly detailed components with great precision [33] and to handle overhangs with minimal-to-no support [34]. Nevertheless, this technology had drawbacks, such as higher manufacturing time and cost than wire-based Directed Energy Deposition methods [35,36]. Additionally, depending on the system used, the size of the component can be limited. On the other hand, wire-based DED techniques, like WAAM (Wire Arc Additive Manufacturing), provide the capability of 3D printing large metal components (i.e., a structural node, a T-joint, etc.) much faster and cheaper comparted to others AM process, which agrees with civil and structure engineering applications. However, WAAM components have less precision in terms of details and surface smoothness.

Few studies have already explored the combination of topology optimization with WAAM. In [37], a comprehensive overview of the potential and challenges of 3D printing with steel, particularly focusing on the WAAM method is provided. It also highlights the applications of WAAM in creating connections, beam reinforcements, and even

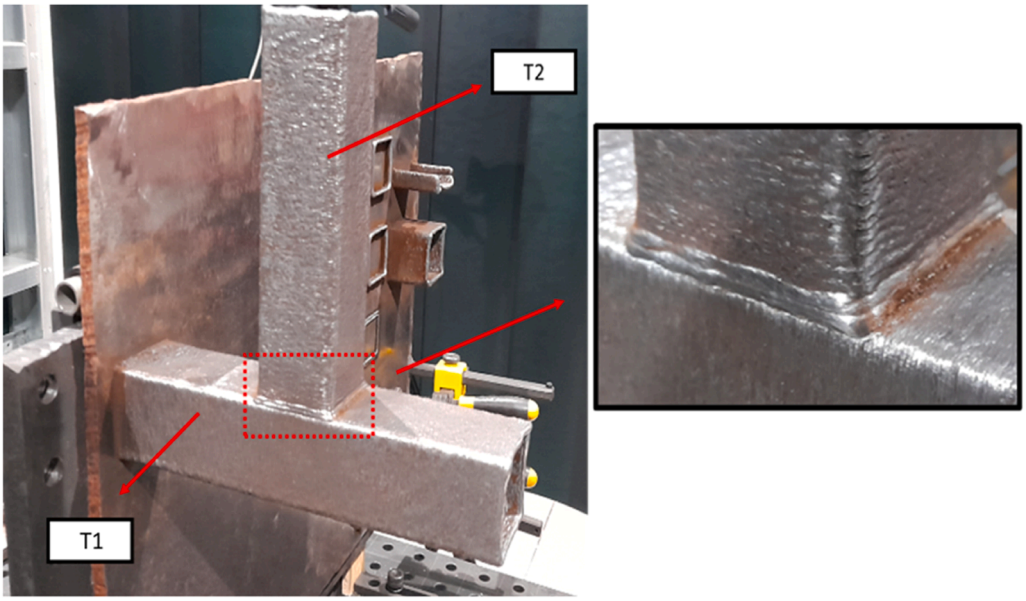

Fig. 6. Non-optimized tubular T-joint.

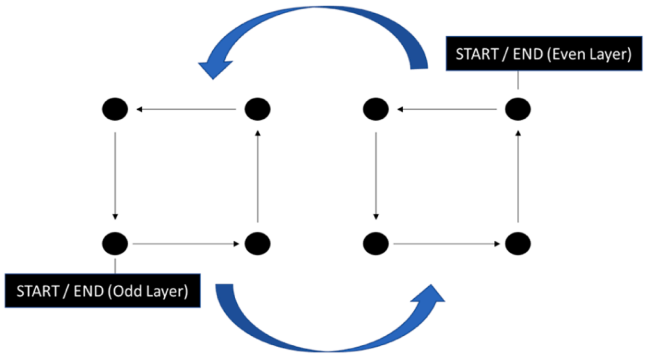

Fig. 7. Printing Sequence.

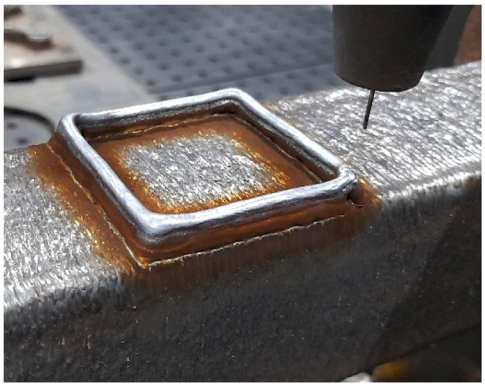

Fig. 8. Transition between tubes.

complete structures like bridges. [38] aims to integrate computational design tools with structural engineering principles to create efficient and structurally optimized elements for construction. It emphasizes the need to consider manufacturing constraints and material properties in the optimization process but it does not include the manufacturing process in the proposed approach. In [39], an end-to-end framework for the additive manufacture of optimized tubular structures is introduced to optimize and manufacture tubular components. Moreover, this framework includes steps such as layout and geometry optimization, cross-section optimization, and inspection of the manufactured trusses. However, the production planning and the challenges during printing were not incorporated, which may have an impact on the final geometry. From this study, some observations are noted: 1) the use of geometry optimization to rationalize the optimized model; 2) the fact that the optimized model is composed of hollow tubular sections with minimum dimensions to reduce the buckling effect (distortion); 3) the re-engineering step redesign the optimized geometry considering manufacturing constrains and 4) the manufacturing challenges and solutions are presented and discussed.

Mishra et al. [40] address the anisotropic behavior of certain AM metals (i.e., austenitic stainless steel), which can be detrimental to a load-bearing component, by doing topology optimization in conjunction with deposition direction optimization.

3. Methodology

This paper explores the integration of design and manufacturing for which a simple tubular T-joint was selected to illustrate the developments. The research was carried out according to the following methodology:

(1) First, a non-optimized model was created and validated using ABAQUS-FEM simulation (further discussed in Chapter 4). The non-optimized model was manufactured using WAAM (Wire Arc Additive Manufacturing) through CMT (Cold-Metal Transfer) [41], with the equipment described in [42]. An experimental test was conducted to obtain the force-displacement curve of the non-optimized model. The numerical simulation was validated based on the experimental results. During testing, DIC (Digital Image Correlation) was used to record global material displacements and to identify critical stress regions.
(2) Using the non-optimized model as a baseline, different TO methods were explored numerically. In the second step, multiple numerically optimized models were generated, aiming to achieve the same stiffness and resistance with less volume and changes in geometry caused by the optimization process. The model with the best force-displacement curve was then selected for the next step.
(3) The feasibility of the optimized geometry was evaluated. Re-engineering and smoothing of the joint geometry were carried

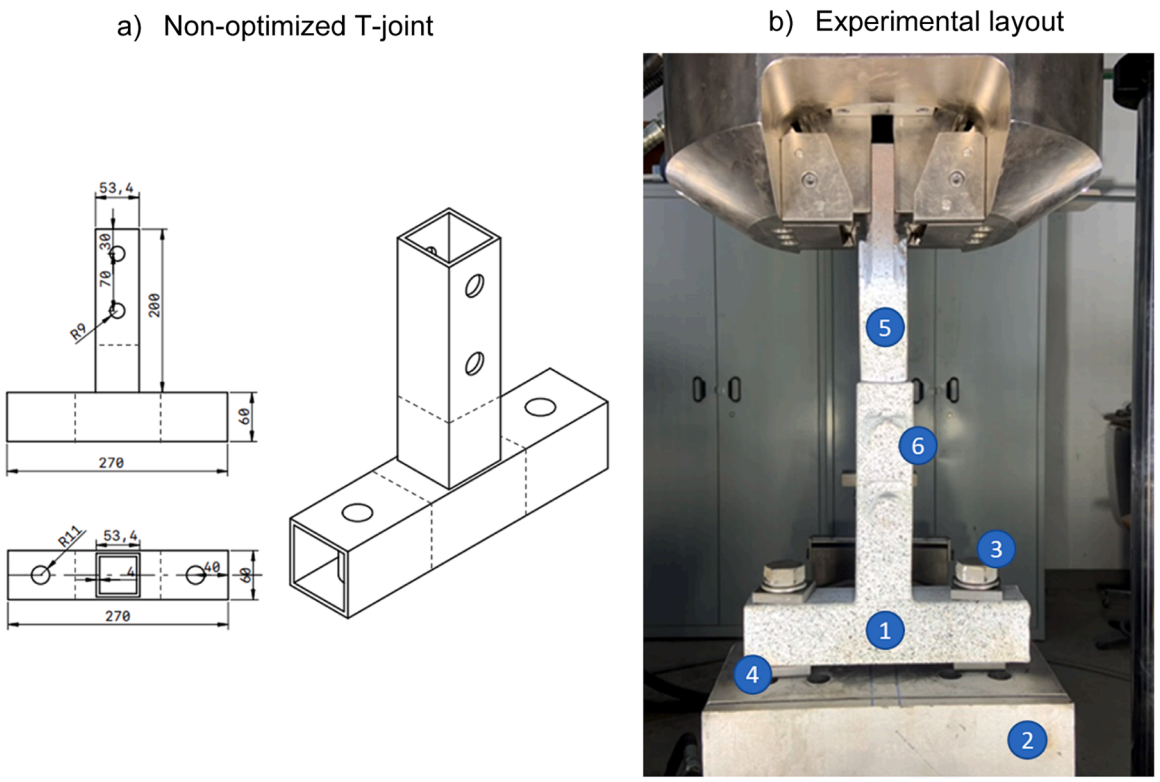

Fig. 9. Geometry and test set-up.

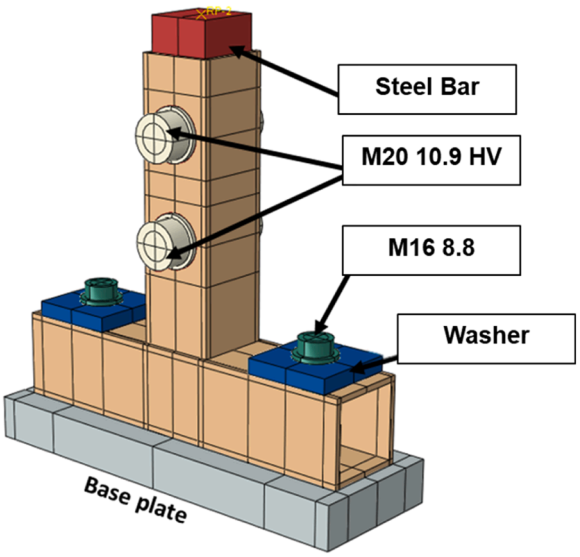

Fig. 10. General view of the numerical model.

out to enable its production. The re-engineered model was validated numerically to determine the impact of the geometry modifications on the mechanical performance.

(4) The optimized geometry was manufactured and tested as the non-optimized geometry in (1).

(5) Finally, the results are compared and discussed.

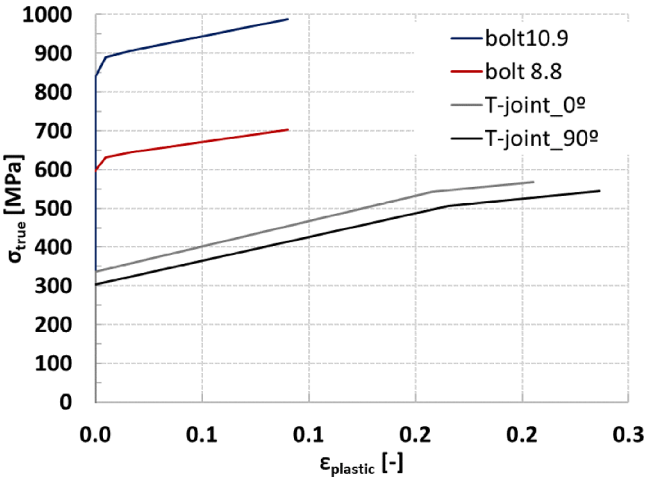

Fig. 11. Stress-strain relationships for plates and bolts.

4. Non-optimized T-joint: analysis and testing

4.1. Additive manufacturing of non-optimized T-joint

The T-joint was fabricated by WAAM (Wire Arc Additive Manufacturing) through Fronius' process: CMT (Cold-Metal Transfer) [41], as described in [42]. The specimen was printed using a mild steel wire (ER70–6). The welding parameters were optimized to land stable 3–4 mm thickness in a single bead-on-plate until a satisfactory output. The selected parameters were: Current 113 A, Voltage 14.3 V, Feed Speed 4 m/min, and Travel Speed 10 mm/s.

The T-joint is illustrated in Fig. 6.. The joint was printed by depositing the material on a table with 0° to build the first tube (T1) with subsequent manufacturing of the second tube (T2) on top of T1 with a

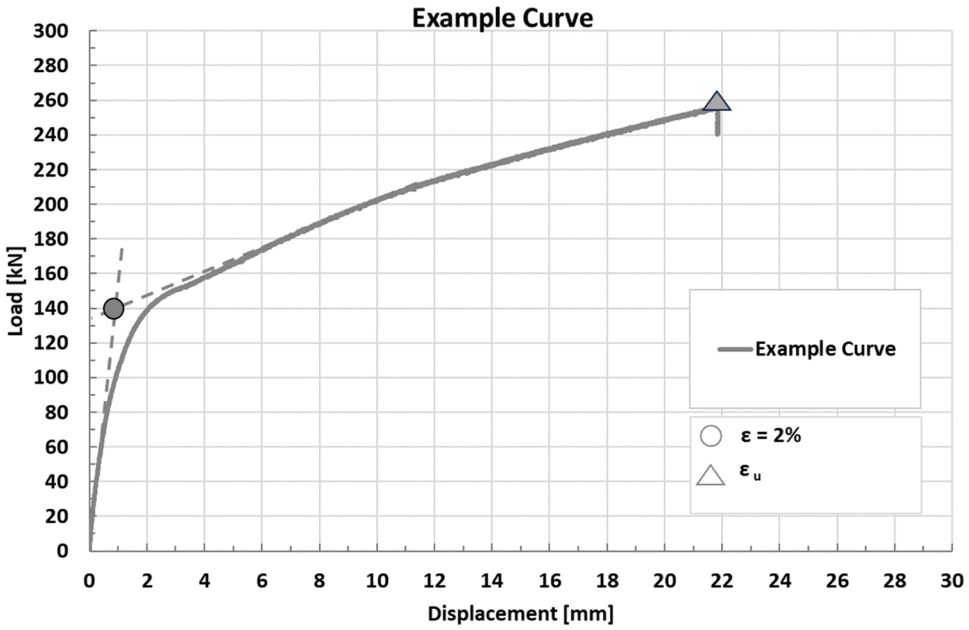

Fig. 12. Example of the data extracted from the force-displacement curve.

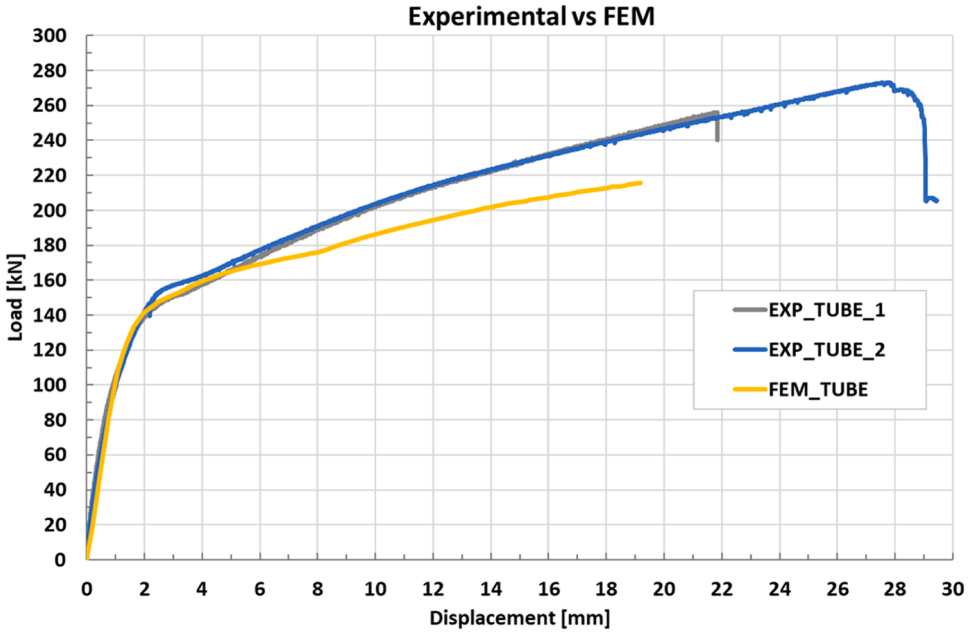

Fig. 13. Force-displacement curve – Experimental test vs FEM.

Table 1
Properties of non-optimized T-joint.

Name	Initial Stiffness	Plastic resistance	Ultimate Load	Volume
	[kN/mm]	[kN]	[kN]	[mm3 x 10^{-3}]
FEM_TUBE	100.78	148.92	-	410.4
EXP_TUBE_1	101.71	137.82	256.05	392.6
EXP_TUBE_2	105.50	150.89	273.16	402.2

90º rotation for the gravity vector to be aligned with the deposition.

To reduce the accumulation of defects due to discontinuities in the deposition (layer's start and end point), the layers were planned to not overlap the welding start positions of each layer by following the sequence shown in Fig. 7.

The two initial layers of T2 were welded with more energy by reducing the travel speed to 5 mm/s, thus allowing for more material in the interface, and the first layer has two bead lines per edge to create a smoother transition between tubes. This phenomenon is visible in Fig. 8.

4.2. Geometry and test set-up

The geometry of the non-optimized T-joint (TUBE) is shown in Fig. 9a, where the T-joint can be described as the combination of 2 square hollow sections, 60 × 60 mm and 54 × 54 mm, fabricated using WAAM. The experimental layout consists of: (1) a T-joint specimen; (2) a T-shape base plate that connects the lower part of the specimen to

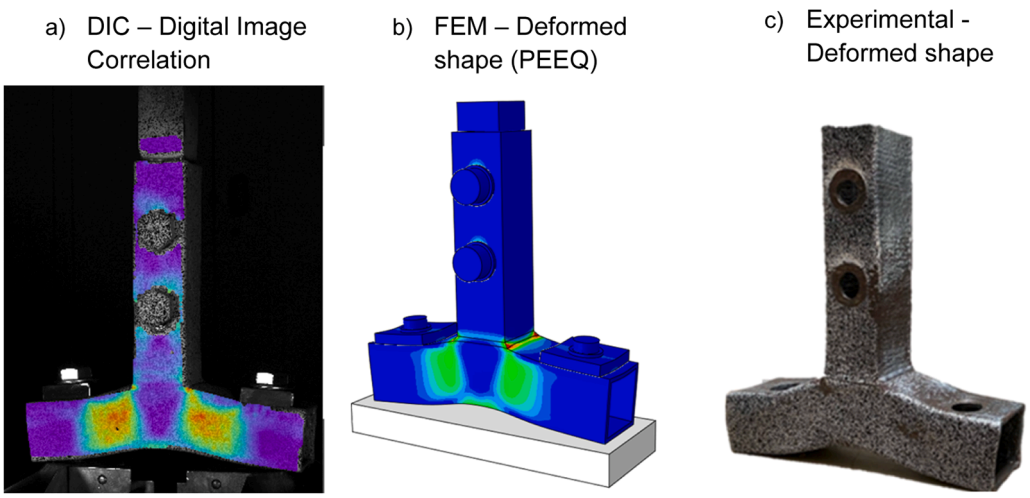

Fig. 14. Deformed Shapes – reference T-joint (TUBE).

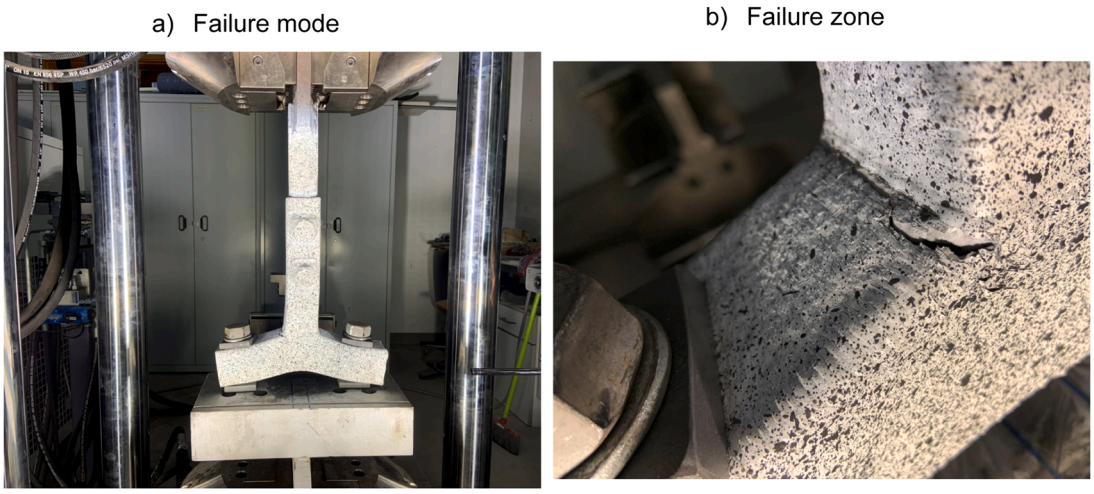

Fig. 15. Failure mode and Failure zone.

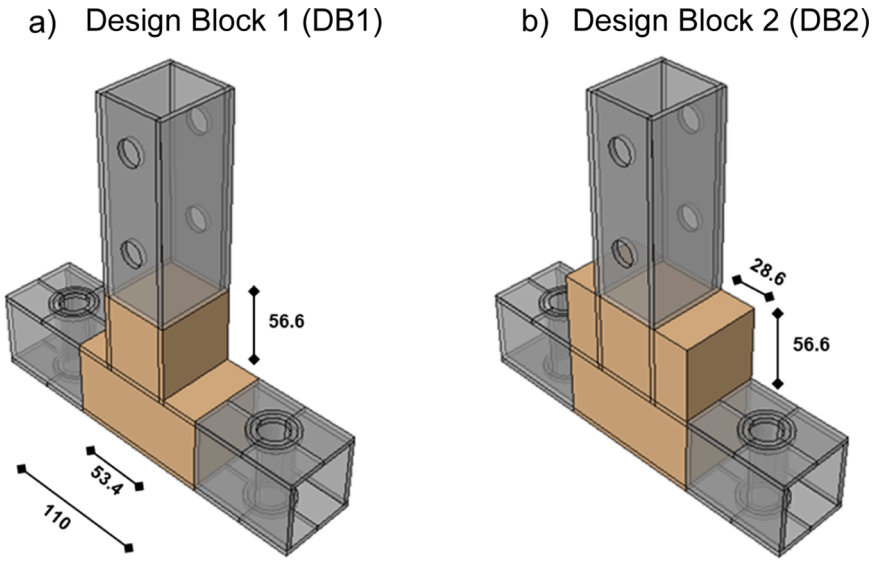

Fig. 16. Design Blocks.

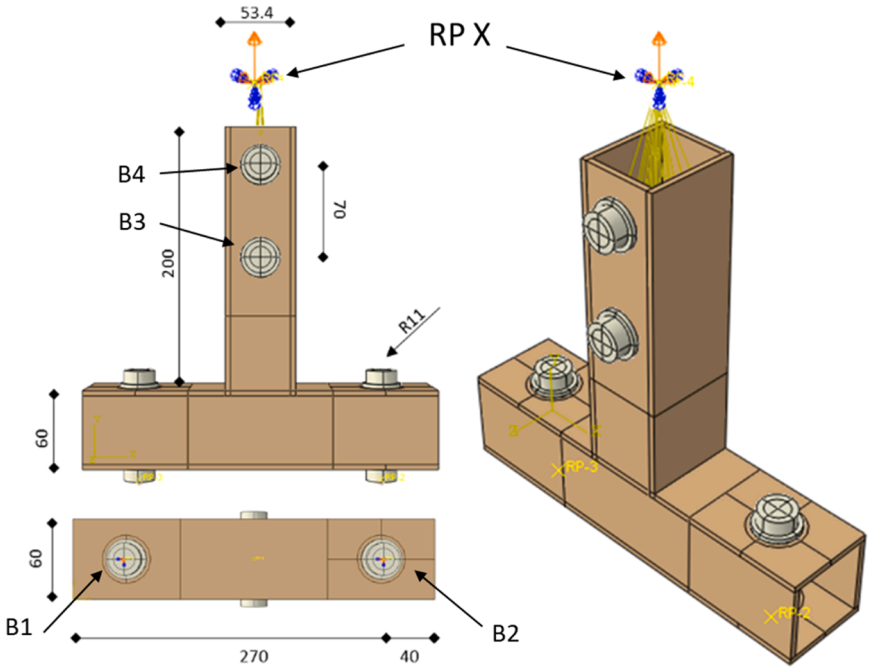

Fig. 17. Optimization model.

Table 2
Optimization process parameters.

Method	Technique	Name	Max n° cycles	Element	Volume Constraint
Sensitivity-based	Default	DEF	50	C3D10	25 %
	SIMP	SIMP	50		
	RAMP	RAMP	50		
Condition-based	-	CB	25		

universal testing machine (Universal Machine W+B LFV 600 kN); (3) two bolts M16 class 8.8 connecting the base plate to the specimen; (4) 4 washers to reinforce the T-joint walls and prevent its deformation (base plate connection); (5) a solid steel bar bolted to the T-joint, which pulls the specimen up; and (6) two bolts M20 class 10.9 that connect the upper part of the specimen to the steel bar (see Fig. 9b). A total of four experimental tests were carried out on this geometry

4.3. Numerical model

A numerical evaluation of the T-joint was carried out with ABAQUS software, using the dynamic implicit solver with the quasi-static procedure [43]. The model corresponds to the experimental layout, comprising: (i) the T-joint; (ii) a base plate (representing the base of the lab machine); (iii) two bolts M16 class 8.8 connecting the base plate to the T-joint; (iv) a couple of washers to reinforce the T-joint walls and prevent their deformation; (v) a solid steel bar bolted to the upper part of the T-joint, used to pull the specimen up; and (vi) two bolts M20 class 10.9 connecting the upper part of T-joint to the steel bar(see Fig. 10). A rigid body constraint was applied to the edge of the steel bar in the direction of the displacement application. The base plate was fully restrained. It is worth mentioning that the design of the T-joint in the numerical model does not considered the surface smoothness of the actual WAAM fabricated T-joint due to the complexity of representing it numerically. This difference can be clearly seen by comparing Figs. 6 and 10.

The model was generated using solid elements, type C3D10, with a "Tet" element shape for the T-joint part and C3D8R with a "Hex" element shape for all the other parts, allowing for non-linear geometrical and material behavior. Normal contact conditions were introduced with "hard-contact" property allowing for separation. Concerning the tangential behavior, the "penalty" formulation of the software was used with a friction coefficient equal to 0.2, translating a typical value for the friction coefficient between two steel surfaces. The simulations were carried out under displacement control by pulling the steel bar up to the failure of the T-joint.

Material nonlinearity was included by introducing a non-linear stress-strain relationship for each material. For the T-joint, the results of the true stress-true plastic strain curves from coupon tests described in [44] were used in 0 and 90° orientation according to the fabrication sequence. Therefore, the properties for the 0° and 90° orientation coupons (T-joint_0° and T-joint_90°) were assigned to the top part and bottom part of the T-joint, respectively. For the bolts, since no coupon tests were available, a trilinear stress-strain law was used with the tensile strength nominal values of bolt class 10.9 and 8.8 (see Fig. 11).

Table 3
Strain Energy x Fraction of Volume.

Name	Strain Energy (N*mm)	Ratio (Initial Strain Energy)	Volume Constraint	Fraction of Volume (%)	Volume ($mm^3 \times 10^3$)
TUBE (DB1)*	6.90E+ 04	100.0 %	-	100.00 %	1704.5
TUBE	8.01E+ 04	116.1 %	-	26.07 %	444.4
CB1	7.59E+ 04	110.0 %	25.0 %	26.15 %	445.7

* Non-optimized T-joint TUBE (DB1) with design block completely solid (see Fig. 16a)

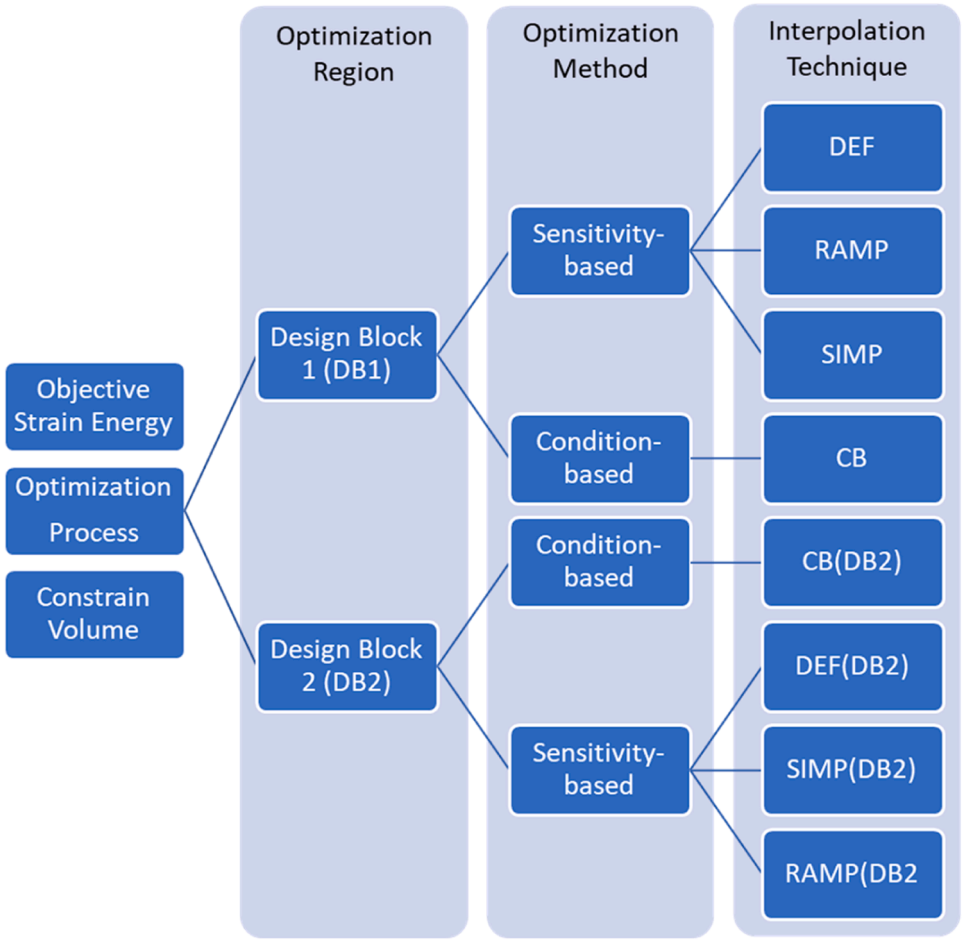

Fig. 18. Optimization Process.

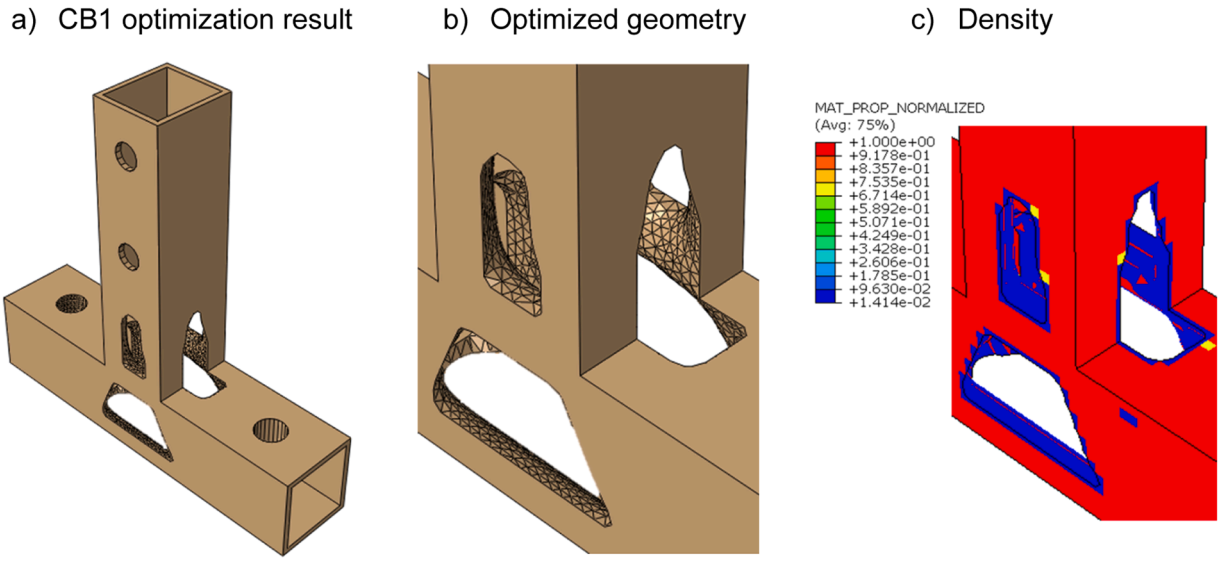

Fig. 19. Comparison between the initial volume parameter.

4.4. Results and discussion

The experimental tests and numerical simulations are primarily compared by force-displacement curves. On these curves, three points are emphasized (Fig. 12): a) plastic resistance, which is obtained by the intersection of two dash lines drawn from linear and plastic section; b) the ultimate load that is highlighted only in the experimental curves as well as the initial stiffness. The latter was computed by averaging the division of the force by displacement of all points of an approximated linear line, represented by the black dashed line in Fig. 12.

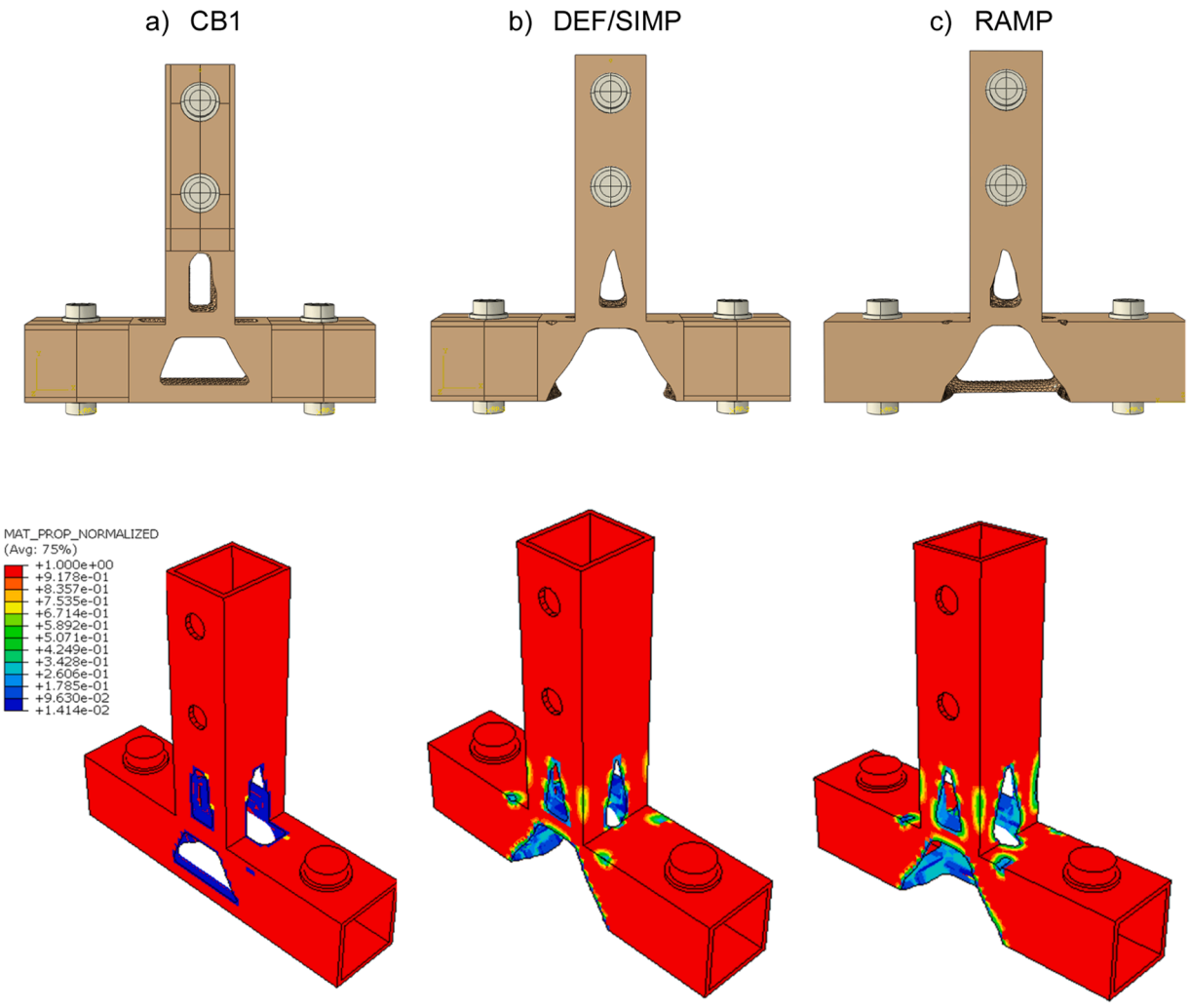

Fig. 20. Initial optimized geometries (25 % of initial volume).

Table 4
Strain Energy x Optimization procedure.

Name	Strain Energy (N * mm)	Ratio (Initial Strain Energy)	Constraint	Fraction of Volume (%)	Volume ($mm^3 \times 10^3$)
TUBE (DB1)	6.90E+ 04	100.0 %	-	100.00 %	1704.5
TUBE	8.01E+ 04	116.09 %	-	26.07 %	444.4
CB1	7.59E+ 04	110.0 %	25.0 %	26.15 %	445.7
SIMP	3.79E+ 05	549.5 %	25.0 %	24.94 %	425.1
RAMP	8.46E+ 05	1226.5 %	25.0 %	25.43 %	433.5

Fig. 13 shows the specimen's experimental and FEM force-displacement curves (TUBE). Two specimens were considered: the first is the exact tubular geometry displayed above (EXP_TUBE_1) and the second is the same geometry but with a reinforcement only in the areas of the circular holes on the top part, which is outside of the optimization region and can represent a 5 % additional volume (EXP_TUBE_2). This reinforcement was placed in order to minimize the chance of premature failure outside of the region of interest due to thickness variation, which happened in EXP_TUBE_1. The results for the parameters defined above are given in Table 1. In general, the numerical model follows closely the experimental results, especially in terms of initial stiffness and plastic strength. The post-elastic resistance is lower than the experimental one, but the deformed final shape is similar, with the plastic deformations concentrated at the transition of the T and at the flange of the T-joint closer to the transition, similar to the deformation usually observed in T-stub connections in tension (see Fig. 14). The difference between numerical and experimental curve may be introduced by the present of significant surface smoothness and thickness variation on the produced prototypes, which is not reproduced in the numerical models and can be observed variability in the volume of this prototypes.

The failure mode is also similar. A crack propagated in the transition zone and bearing of the upper holes is visible, which is shown in Fig. 15. The Digital Image Correlation results also match the numerical simulations, demonstrating accurately its behaviour under tension (see Fig. 14).

5. Topology optimization of T-joints

5.1. Definition of the optimization objective and parameters

5.1.1. Numerical model

The topology optimization was performed using the software

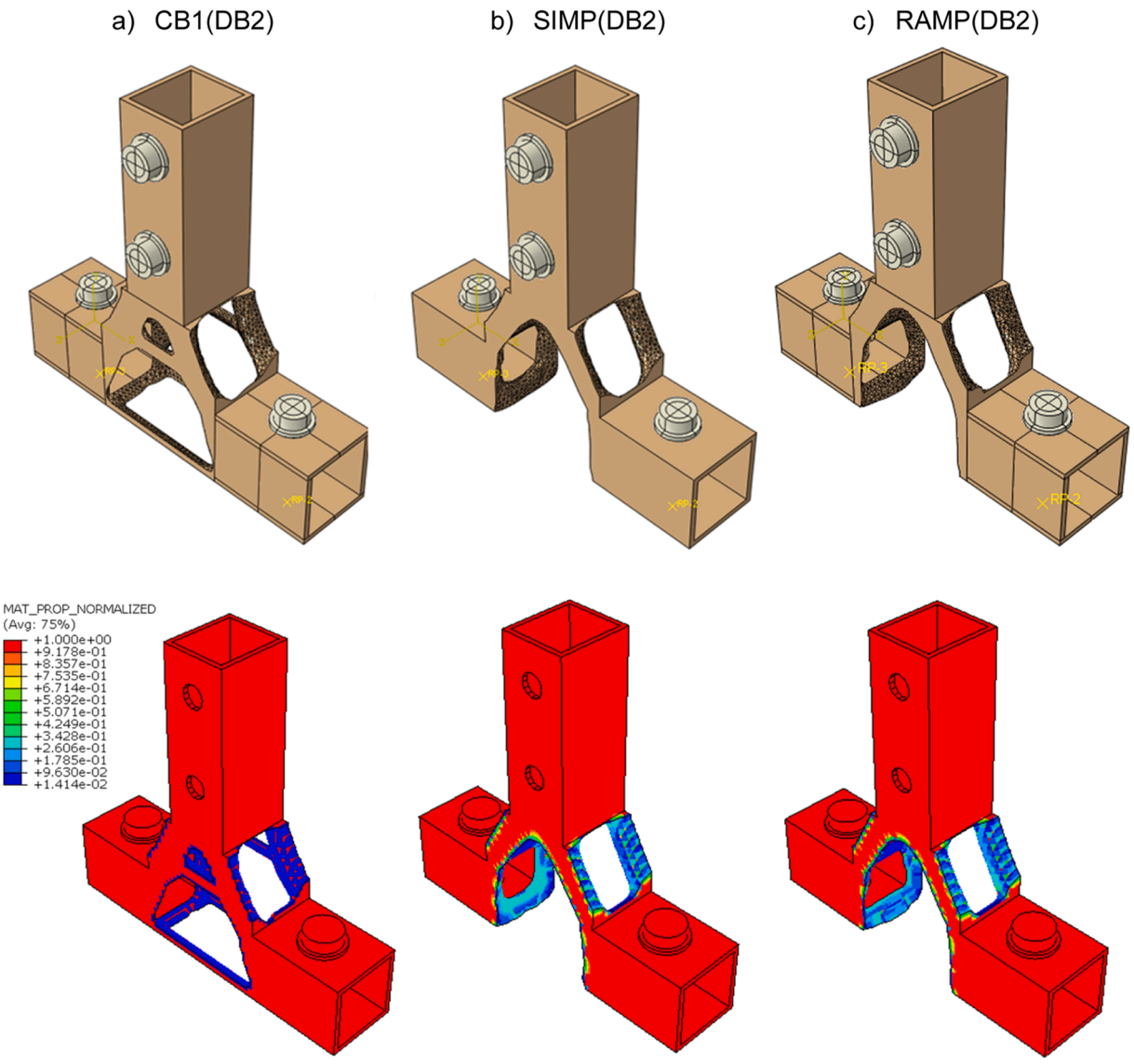

Fig. 21. Optimized shapes from the Design Block 2.

Table 5
Strain energy x Fraction of the volume for DB2.

Name	Strain Energy (N * mm)	Ratio (Initial Strain Energy)	Constraint	Fraction of Volume (%)
TUBE (DB2) *	6.66E+ 04	100.0 %	-	100.0 %
CB1 (DB2)	7.63E+ 04	110.0 %	10.0 %	11.3 %
SIMP (DB2)	3.76E+ 05	549.5 %	10.0 %	9.9 %
RAMP (DB2)	3.75E+ 05	563.47 %	10.00 %	9.95 %

TOSCA/ABAQUS [21]. The numerical model was created according to the modelling assumptions previously described in section 4.3. For the definition of the optimization problem, it is required to specify the optimization method, the optimization region, apply constraints, and specify the optimization function. Moreover, two parameters were investigated: the optimization region (optimization block) and the types of optimization method.

For the optimization region, two alternatives were considered: i) a solid block (DB1) in the intersection zone of the T-joint (see Fig. 16a); or ii) an alternative larger solid block (DB2), which provides a larger and less constrain design space (see Fig. 16b).

In comparison with the model presented in section 4.3, simplified boundary conditions were applied to save calculation time. The joint is connected by four bolts in the zones that cannot undergo any modification, non-design regions. The bottom of the bolts (B1 and B2) on each side of the connection is restrained from translation and rotation in all directions. The bolts on top (B3 and B4) are coupled to a reference point X. The load of 100 kN is applied at the RP X, the rest of the degrees of freedom are restrained (see Fig. 17). The magnitude of the load was selected regarding the force-displacement curve of the non-optimized tube, approximately 2/3 of the load corresponding to the elastic region.

5.1.2. *Topology optimization procedure*

The software ABAQUS has two methods for topology optimization: sensitivity-based and condition-based optimization. The sensitivity-based optimization [18] modifies the stiffness and density while trying to achieve the objective function and satisfying the constraints. Moreover, for this method in ABAQUS, three material interpolation techniques are available: Rational Approximation of Material Properties (RAMP), Solid isotropic material with penalization (SIMP), and the ABAQUS default (DEF), a SIMP variation. In contrast, condition-based

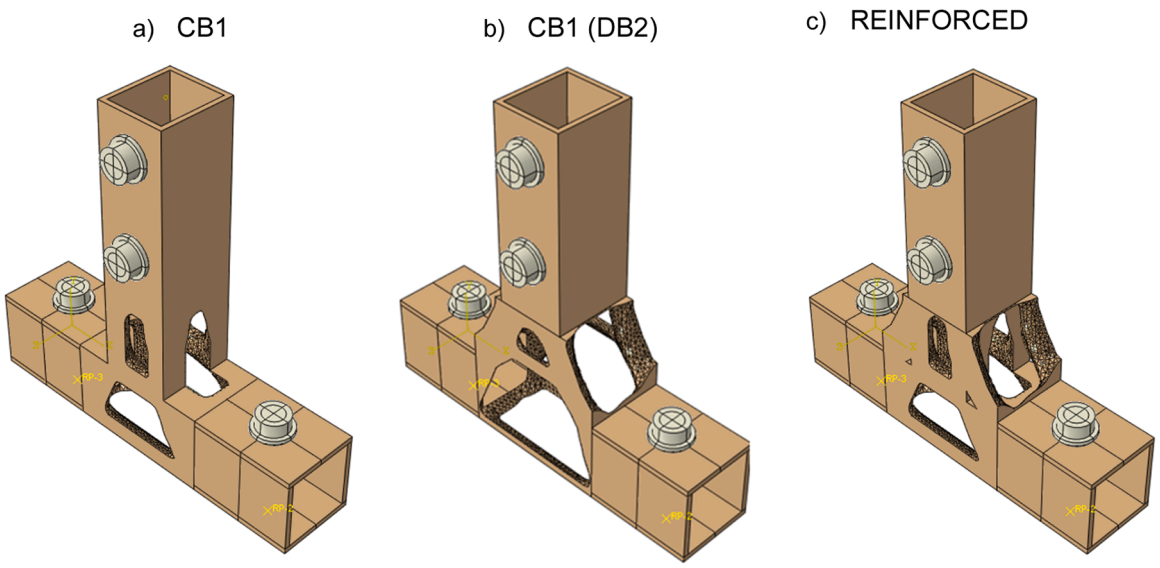

Fig. 22. Reinforced joint.

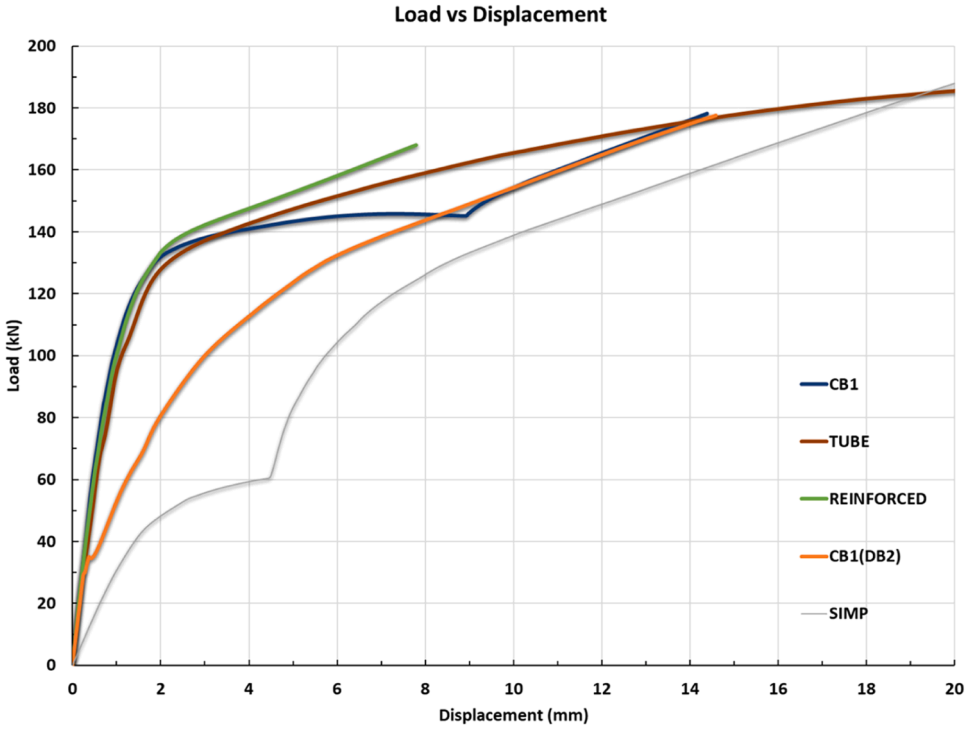

Fig. 23. Load vs displacement curve for selected t-joints.

Table 6
Parameters of selected T-joints.

Name	Initial Stiffness	Plastic resistance	Resistance Load at $\varepsilon = 0.05$	Volume
	S_i [kN/mm]	Fy [kN]	Fy [kN]	($mm^3 \times 10^3$)
TUBE	114.48	137.63	142.87	444.4
REINFORCED	122.37	134.727	145.39	476.4
CB1	116.90	133.38	139.12	428.4
CB1(DB2)	63.39	75.11	83.56	448.8
SIMP	32.12	51.51	52.89	425.1

optimization (CB) [19] uses the strain energy and stresses at the nodes instead of the local stiffness. All of these alternatives are considered in the model to find the optimal topology.

The objective function is set as the strain energy of the whole model, given the relationship between stiffness and strain energy the procedure attempts to minimize strain energy, maximizing the stiffness, using the volume as the constraint. As the design block 1 of the optimization model is solid, this constraint assumes the value 25 % to be similar to the l volume of the equivalent region in the non-optimized hollow T-joint.

Since the above-mentioned procedure is performed for linear elastic material and the objective function aims to satisfy the stiffness requirement, there is no information regarding the resistance of the joints. Hence, after each TO geometry was obtained, large displacement

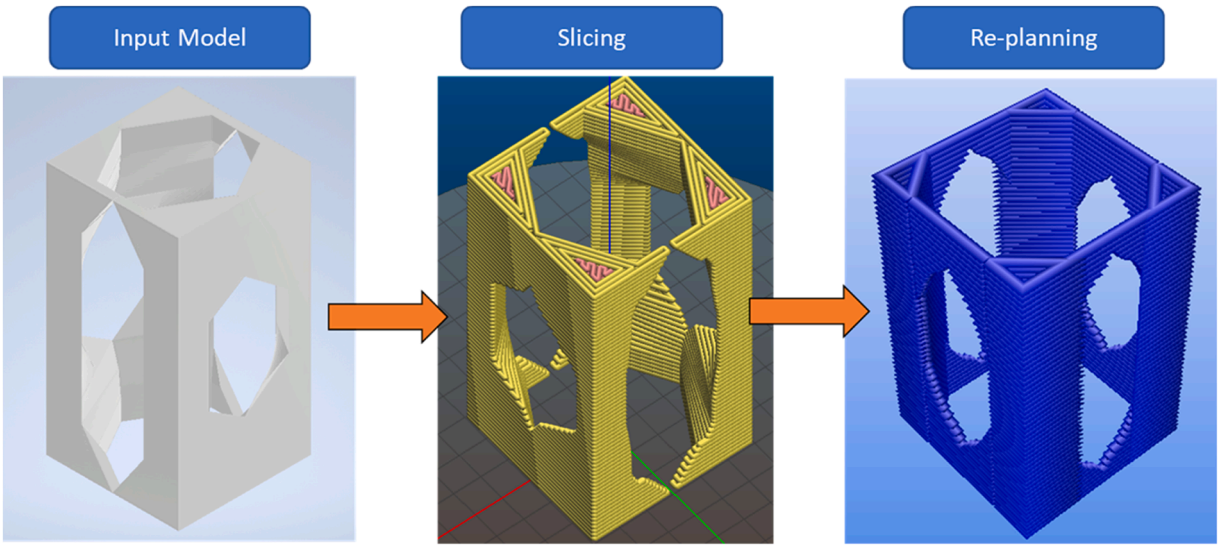

Fig. 24. Transition from geometry to virtual weld beads.

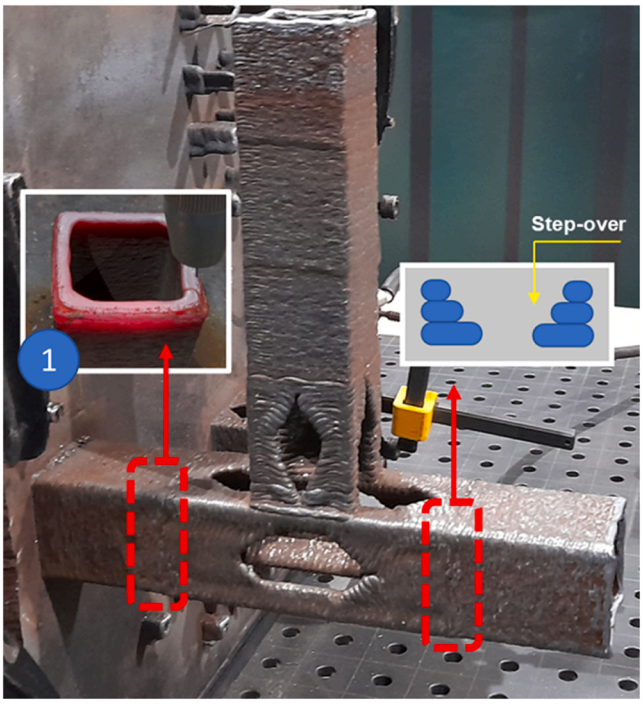

Fig. 25. Connection between non-design and design region.

materially non-linear analyses were performed to evaluate the impact of plasticity for the selected geometries. These analyses are implemented with the material properties given in Section 4.3 (using the T-joint_0 for the top part and T-joint_90 for the bottom part) and are further referred to as plastic analysis. The validations were carried out under displacement control with 20 mm applied displacement, similar to the non-optimized T-joint as described in Section 4.2. Further information about the optimization process is shown in Table 2. A flowchart of the optimization process is presented below.

To assess the influence of these parameters, they are firstly compared separately and then combined together in the final optimization. The optimization procedures are evaluated and compared by the stress levels, the optimized geometry, and structural behaviour, which is obtained by a plastic analysis (validation) using ABAQUS (Finite Element Methods – FEM). This study evaluates: (1) the two optimizations methods available in TOSCA including their material interpolation technique, (2) the volume constrains set at 25 % of the volume, which is similar to the regular T-joint and (3) the two design blocks discussed in Section 5.1.1, where the optimization occurs.

5.2. Comparative analysis of results

5.2.1. Reference case

Firstly, a reference case was analysed which is later used for comparison of the optimization results to assess the efficiency. The results of the relation between strain energy and reduced volume are given in Table 3 that compares the reference solution (TUBE) with the optimized solutions using the CB algorithm. The TUBE(DB1) below represents the model before optimization, which has the optimization region has a solid block, so its volume is considerably higher than others. A constraint of 25 % was selected for the optimization region, the final output geometry would have a similar volume to the FEM_TUBE.

Fig. 18 demonstrates the resulting geometry and the density of the mesh by a range of colours from red (density = 1.0) to dark blue (density = 0.0).

5.2.2. Influence of the optimization procedure

In this section, the different optimization algorithms (sensitivity-based with three material interpolation and condition-based) are assessed assuming the same fraction of volume (25 %). Fig. 20 depicts the results of the four algorithms (CB, DEF, SIMP and RAMP). The DEF and SIMP techniques converged to identical shapes, where no material is placed at the bottom of the tube. The RAMP converged to a geometry between the DEF/SIMP and the condition-based algorithm (CB1). Furthermore, the last row of Fig. 19 illustrates the density in each element of the mesh that agrees with the optimization procedure, in which SIMP and RAMP have a significant number of intermediate elements compared to CB1 demonstrating the tendency of the condition-based optimization to a binary density.

As the CB1 T-joint exhibits the most consistent optimized geometry and the best minimum strain energy between all attempts, this model is henceforth used (see Table 4)

5.2.3. Influence of the design space

In this section, the influence of the design block (Fig. 16) on the optimized shape is assessed. The results of the different methods are compared analysing the results of the Design Block 2. DEF and SIMP lead

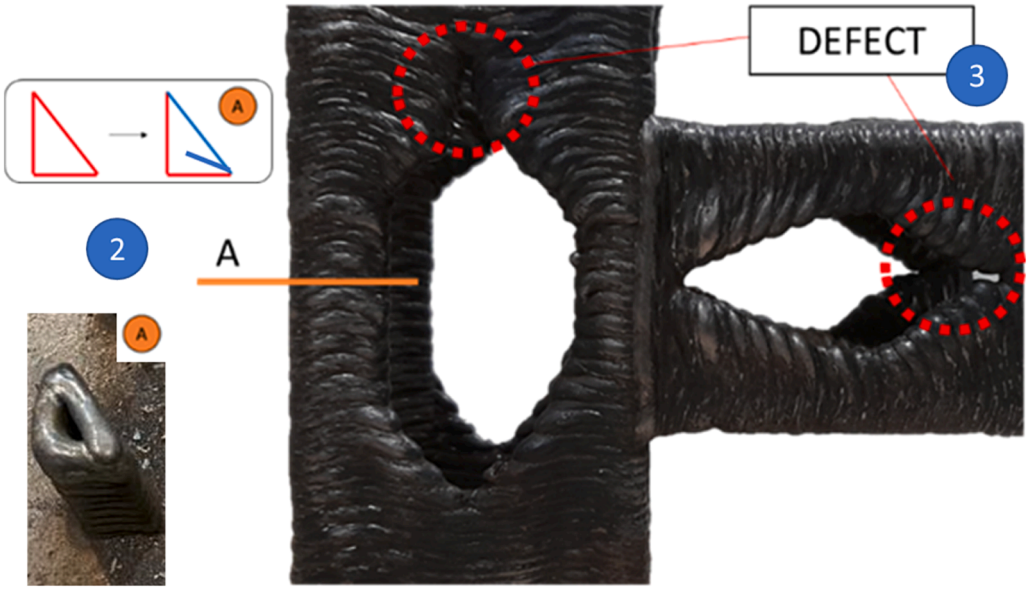

Fig. 26. Re-planning outcome.

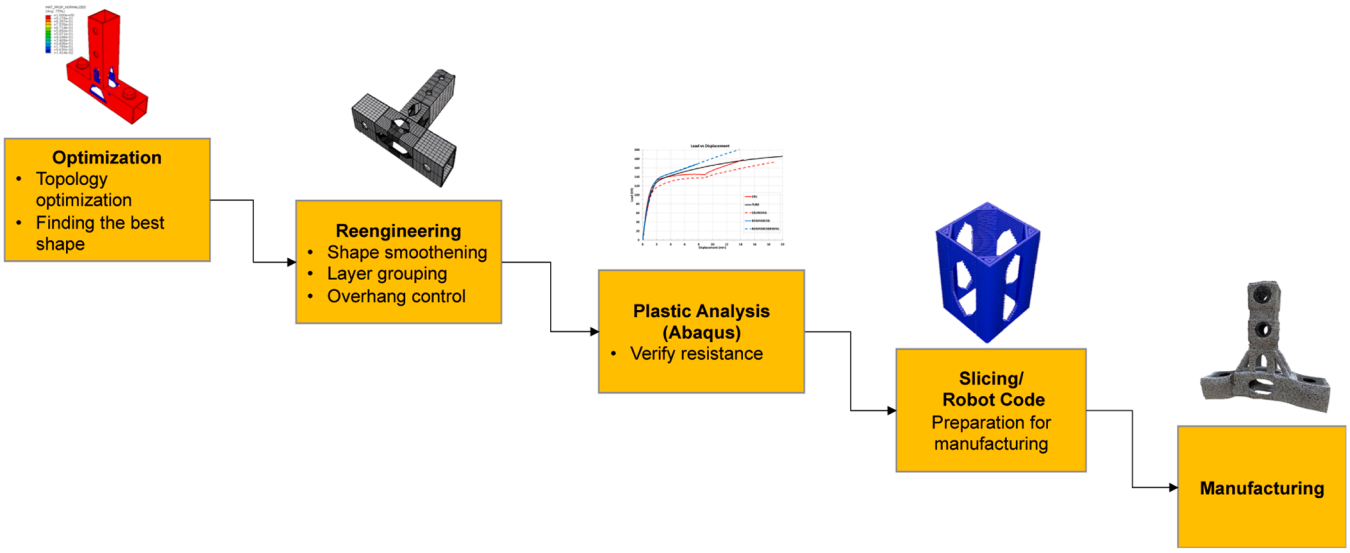

Fig. 27. Adopted workflow.

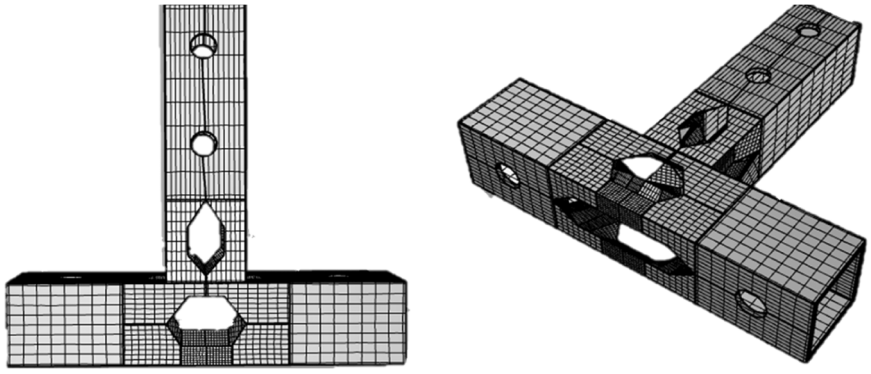

Fig. 28. Optimized joint during the re-engineering (RHINO7).

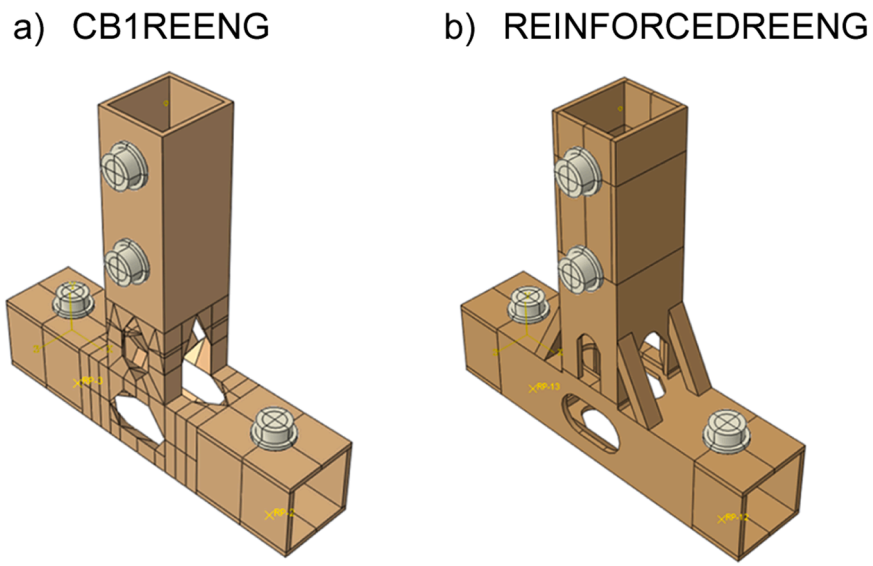

Fig. 29. Optimized joints after re-engineering.

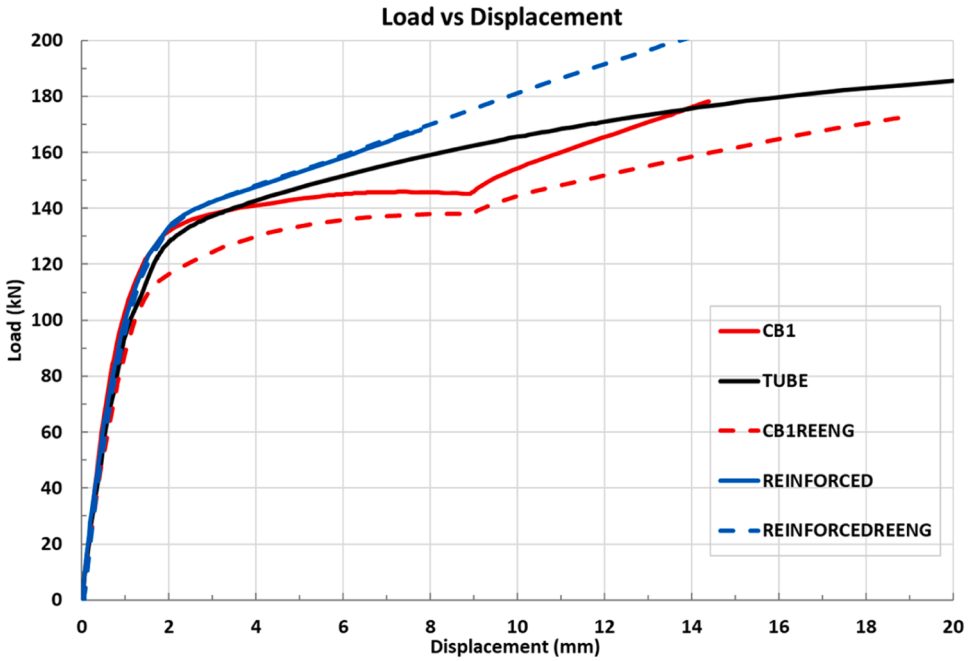

Fig. 30. Load vs displacement curves of reengineering t-joint.

to very similar results as Design Block 1, where no material is left in the bottom part of the joint. All material is directed to the top to form an inverse "V" shape connecting the sides to the top part.

CB maintains a link between the two bottom sides, which is structurally more stable (see Fig. 21). However, the optimized geometries are very thin and prone to instability, which was confirmed by the nonlinear analysis. This is illustrated by the load-displacement curve of the alternative design block and the lower strain energy (see Table 5).

5.3. Reinforced geometry

Although the performance of the Design Block 2 (DB2) was not desirable, the larger design space might lead to a better-optimized shape. Hence, the CB optimization of both design blocks was combined into a single joint to verify if the members in the added design space could lead to improved performance. The new optimized joint is called "REINFORCED", shown in Fig. 22.

The new geometry was created by combining the results from CB-optimized shape from DB2 and CB1 using a smaller design block. Fig. 23 compares the force vs displacement curves for the reference joint and the three optimized solutions. For each curve, the corresponding Plastic load and load corresponding to 5 % plastic strain were calculated according to the definition in Fig. 12. Table 6 compares the corresponding parameters. The CB1(DB2) curve presents a hardening response at about 60 kN, corresponding to the contact of the hard contact of the bolts that fix the bottom tube. The same occurs for the other optimized solutions, albeit in the post-limit range, already over the plastic resistance of the joint. The nonlinear plastic analysis revealed promising results regarding its mechanical behaviour compared to the TUBE (see Fig. 23 and Table 6). However, the reinforced joint has more volume than the tube due to the addition of material. Finally, CB1 and REINFORCED were selected for the next step.

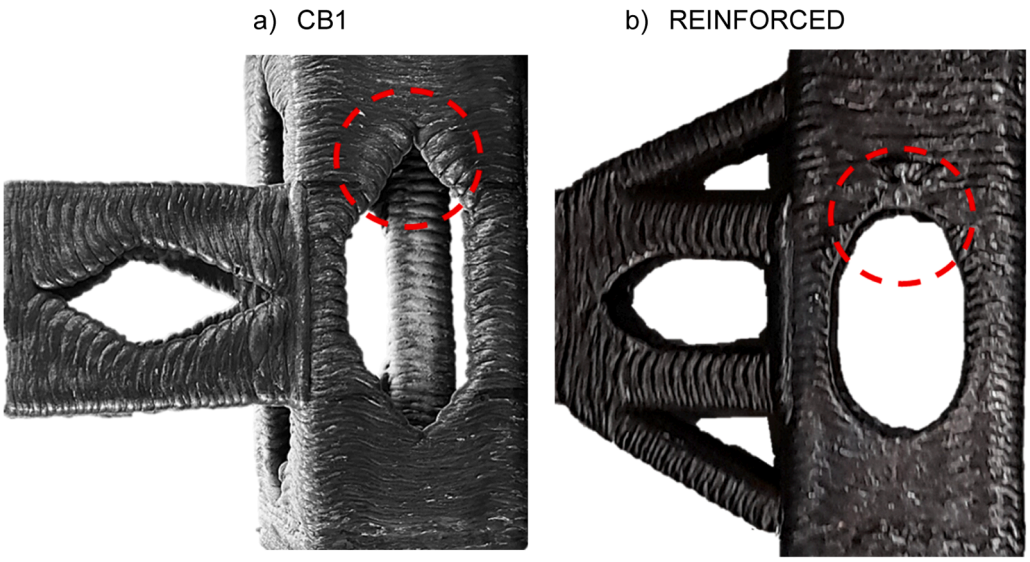

Fig. 31. Manufacturing of CB1 and REINFORCED.

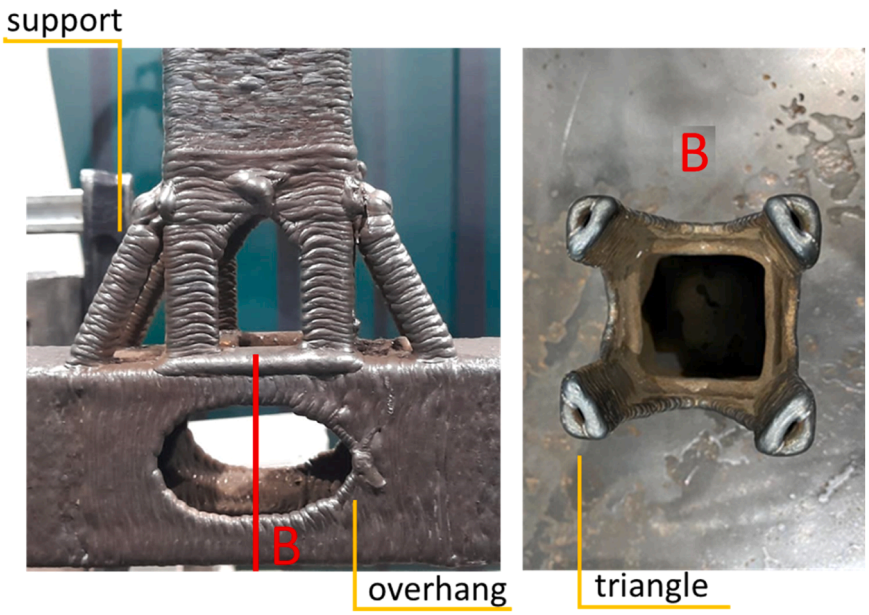

Fig. 32. Manufacturing of optimized design region.

5.4. Summary

In this section, several TOs were carried out varying – the design region, TO method, and constraints. It was shown that depending on the inputs, the results may vary significantly. Based on the results obtained, it was concluded that:

- CB1 gave better results than SIMP regarding their force-displacements curves.
- Larger design space may lead to the most efficient solution, since the TO algorithm has more possibilities to remove elements.
- Combination of optimizations can result in a better geometry.

6. Manufacturing of TO joints

6.1. Manufacturing challenges

After the topology optimization, ideally the part is directly manufactured. This is not always possible due to the manufacturing constraints which are present in every process. In this section, the translation from geometry (CAD) to the final part is discussed. The geometry resulting from the simulation was modified to make it as smooth as possible (Input Model), then it is divided into layers (Slicing) where in each layer the toolpath is specified depending on the thickness of the weld and finally converted into robot code which is used for manufacturing (see Fig. 24).

The slicing procedure is conducted using the software Slic3r, which is originally developed for polymer 3D printing. Hence, it does not have the flexibility to consider some of the features related to metals such as variable bead geometries and distortions inherent to WAAM. Therefore,

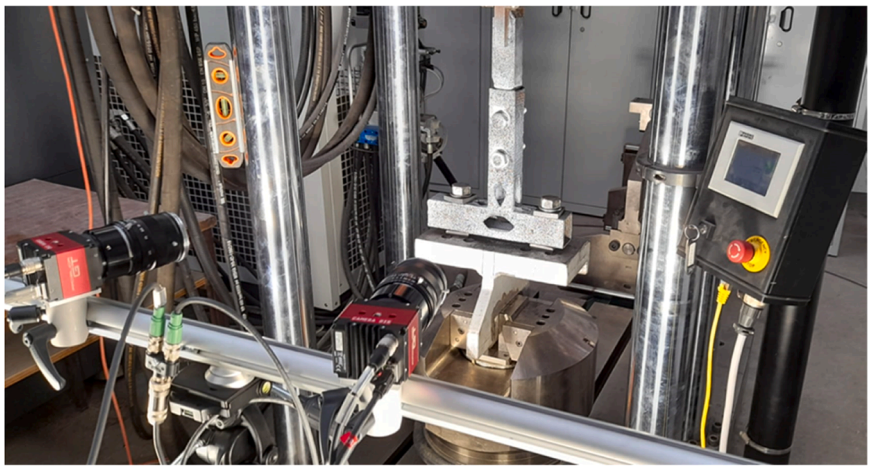

Fig. 33. Experimental test of the optimized T-joint CB1.

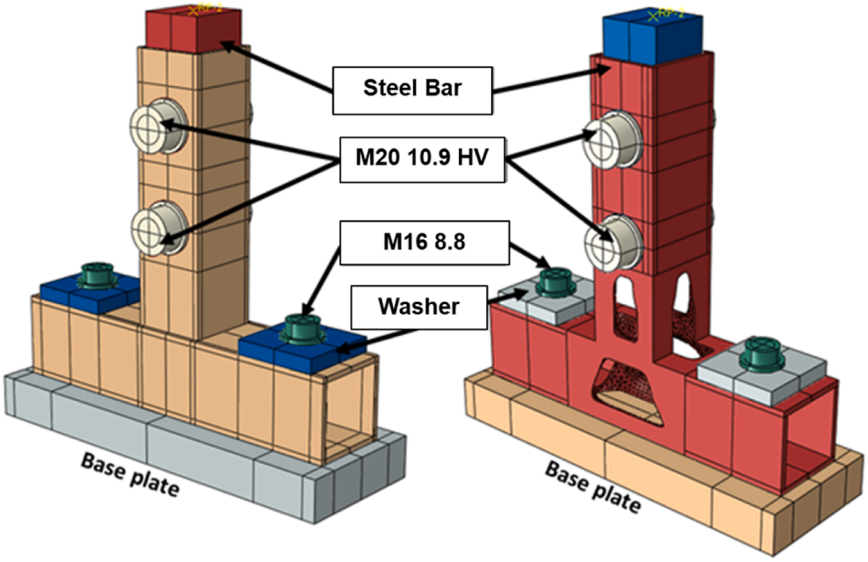

Fig. 34. General overview of the numerical model of optimized T-joint CB1.

a re-planning is required to adjust the layer's sequence and material placement, and re-plan trajectories considering TCP (Tool Centre Point) tool orientations and possible collisions.

The re-planning focused on grouping similar layers and on performing validations with experimental campaigns to better define the weld-on-weld coordinates and interactions such as step-over and overlap distances. The initial approach focused on manufacturability, applying looser criteria for geometry accuracy. For the first optimized T-joint, there are three sensitive areas:

- Transition between tubular part and optimized part (1) – Fig. 25.
- Maintaining the stability of the thinnest parts of the optimized part (2) are further referred to as *triangles* – Fig. 26.
- Overhangs in optimized part (3) – Fig. 26.

The first area *Transition between optimized and non-optimized zones* causes a problem for fabrication because of the difference in thickness and geometry between the tube and the optimized part triangles (see Fig. 25). In this case, the difficulty arises from the fact that there is no material to support the diagonal line of the triangle shape in the optimized part, hence a transition was added in the shape of a reverse pyramid shape to gradually extend to the optimized geometry. These layers were accomplished by adjusting the step-over and adding a slight tool angle to weld towards previously welded material. This same transition is added to the top of the lower tube, now as a pyramid for symmetry.

The other challenges are internal triangular structures (see Fig. 26) mainly due to their size (≈14x10mm), internal infill and sharp angle (≈30°) which lead to several issues such as accumulated material and poor corner definition if produced directly from the slicing. The solution was to split the triangle into two paths (represented in Fig. 26 with a blue and red colour at Letter A). Through this approach and by changing the weld direction between layers, it was possible to retain the corner shape more accurately, minimizing the accumulation of error in a specific corner.

Yet, there was a problem with the infill path that caused more material to accumulate internally; this is explained by the short length of the welding trajectory that caused material accumulation due to localized heat input. This situation was avoided by executing two "L" paths before an "infill" path (two red lines before a blue line in Fig. 26).

Another critical problem that limited manufacturing was the presence of overhang features (Fig. 26). Even though uniformization was applied to the geometry during the re-engineering that restricted the angle of the overhangs, there is still a need for tool angles because of

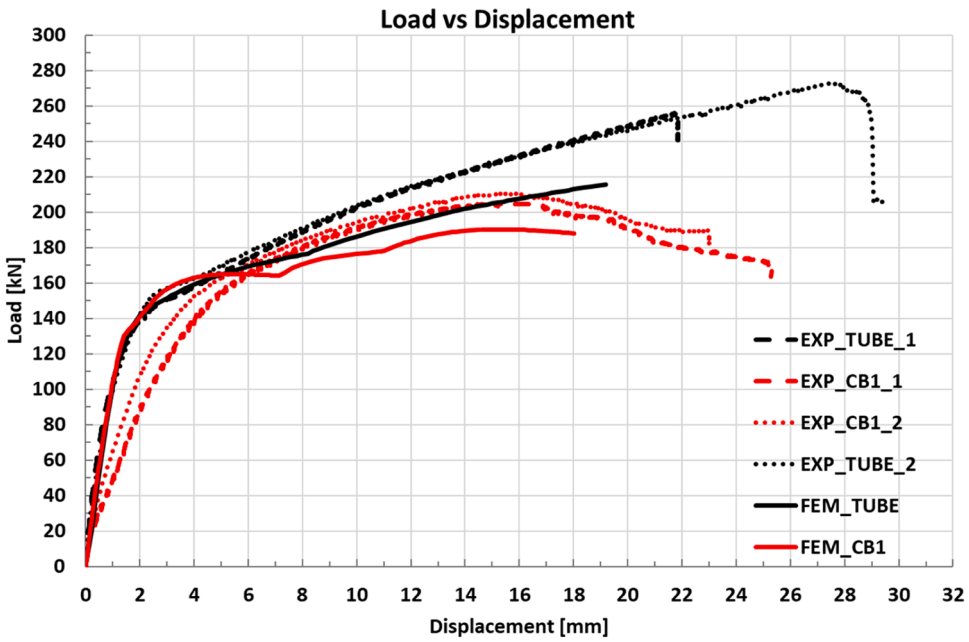

Fig. 35. Non-optimized vs. CB1 T-joint – Load vs displacements curves.

system limitations. In this case, tool inclination was applied which approximately aligns the tool perpendicular to the edge line of the overhang in combination with alternating start and end points. The adopted strategy was a gradual convergence of structures using inclinations that would eventually join. Nevertheless, the final appearance of the overhang structures was not identical to the CAD.

6.2. *Adopted procedure*

As discussed in the previous section, the optimized geometry from ABAQUS software is not directly suitable for additive manufacturing because of irregularities such as small curves and angles and limited thickness. In addition, it was shown that in several steps the geometry has to be reconsidered to avoid manufacturing challenges. Hence, the application of the ideal workflow shown in Fig. 1 is not applicable. The irregular geometry enforces the use of different production parameters which can result in iterations between the initial CAD model, Slicing and Production planning, as previously discussed Fig. 2. Consequently, the workflow must include (see Fig. 27):

- *Re-engineering* aiming at the consideration of several parameters within the CAD stage thus avoiding iterations related to the geometry.
- *Manufacturing* which considers challenging geometrical features and discusses the way to tackle them.

6.2.1. *Reengineering*

To simplify the printing process and rationalize the topology optimization output, the CB1 and REINFORCED models were re-engineered using the software Rhino7 [45]. This process involves adjustment of the geometry into regular and repeated shapes keeping the initial volume as target. All curves in the optimized geometry are smoothened to produce a geometry which respect a minimal inclination of 45º and thickness of approximately 4 mm (see Fig. 28); these restrictions were applied considering the manufacturing limitations. Yet, the reengineering is not limited to simply smoothening the geometry, but it also considers the generation of a geometry as symmetric as possible to simplify the re-engineering, stress distribution, and pre-printing procedure, which considers slicing and path planning.

As part of the reengineering process, it is necessary to run plastic analysis in Abaqus in order to validate that the reengineered geometry still satisfies the requirement for strength and stiffness of the part. Consequently, if it behaves similarly to the CAD geometries it is approved for manufacturing (see Fig. 29). The Reinforced Reengineered (REINFORCEDREENG) joint was not weakened by the process, besides the removal of material. In contrast, the CB1 Reengineered (CB1REENG) was affected by the process due to changes in the geometry related to printing limitations at the time.

Fig. 30 shows clearly that the REINFORCEDREENG achieved a better performance when compared to the reference solution, with a lower volume of material. REINFORCEDREEENG and CB1REENG are further referred to as REINFORCED and CB1, respectively.

6.2.2. *Manufacturing*

This printing process was further improved by employing overhang support constructed by spot welding, which was applied in the REINFORCED joint. The spots were welded on each side until they met in the centre. After a cooling period, the material was carefully deposited on top of it, considering heating and fusion penetration. A pleasing round shape was constructed that solved the previous overhang issues (see Fig. 31).

A further challenge in the printing process of the REINFORCED joint was the support structures connecting the bottom to the top part (see Fig. 32). The approach was to manufacture the support with a specific angle until it was close enough to the top part to implement a different deposition trajectory. The welding path was adjusted to cross the triangle and support in a single weld, enforcing a solid connection between them.

7. Experimental and numerical assessment of optimized joints

7.1. *Experimental tests*

The experimental tests comprised a total of 4 optimized specimens: two CB1 optimized t-joints, and two REINFORCED optimized t-joints, in addition to the reference T-joint. They are subjected to the same tensile test procedure described in Section 4.2 (see Fig. 33).

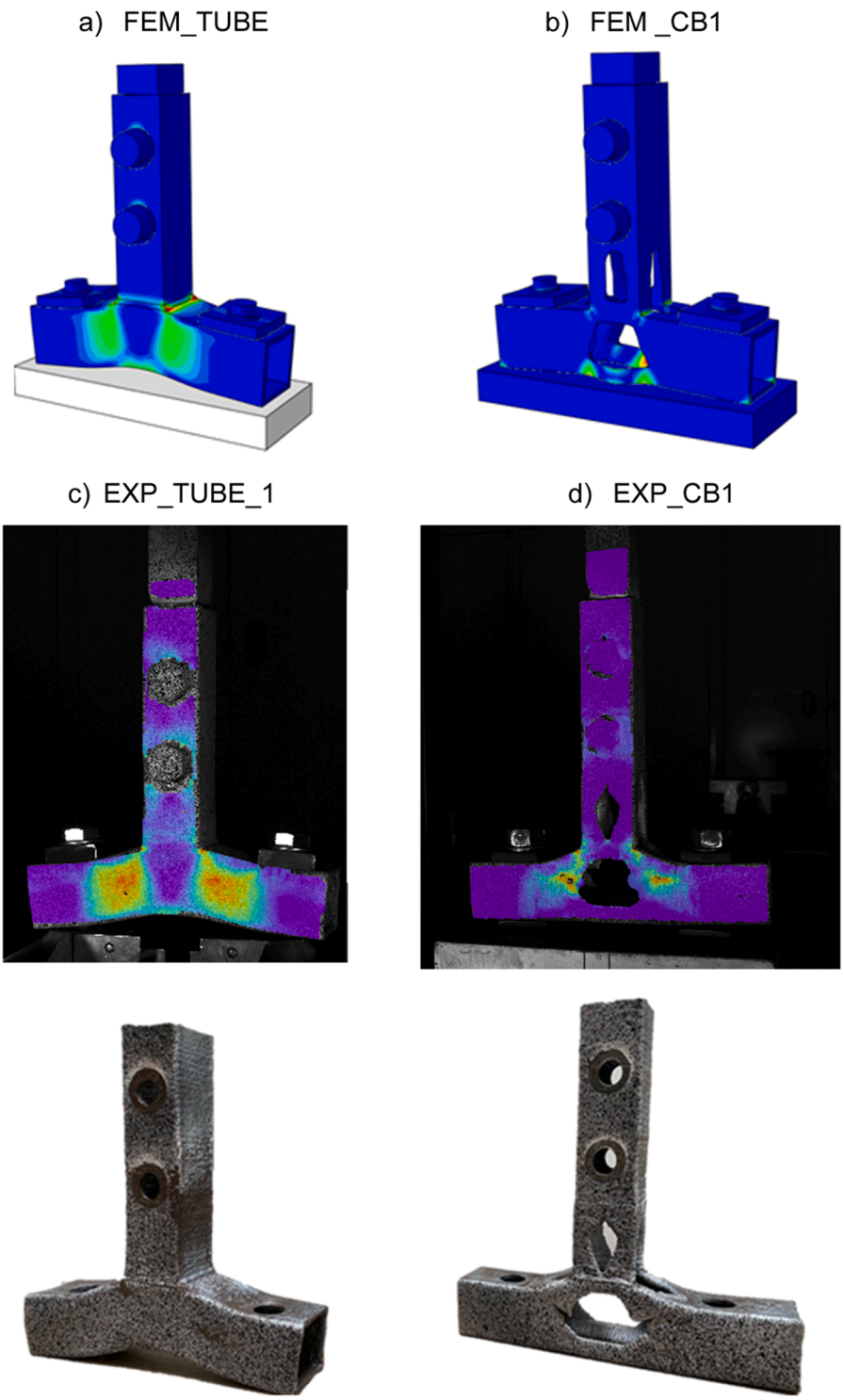

Fig. 36. Non-optimized vs. CB1 T-joint – Deformed shapes.

7.2. Numerical models

The numerical simulations for CB1 and REINFORCED T-joints consisted of the same FE model as the regular T-joint, specified in Section 4.3 (see Fig. 34).

7.3. Results and discussion

This subsection analyses and discusses the results of the two final optimized solutions CB1 and REINFORCED with the reference T-joint. Fig. 35 compares the CB1 T-joints and the reference T-joints both in terms of the experimental test results and the numerical simulations. Firstly, as already reported in Section 4.4, the experimental and the numerical curves for the TUBE T-joint show perfect agreement up to the plastic resistance and until a plastic displacement of about 5 mm, (approximately 10 % of the maximum equivalent plastic strain).

The numerical results for CB1 also coincide with the TUBE up to that level of deformation. However, a significant difference is observed in the two CB1 experimental results in terms of the initial stiffness. This happened due to the defects of the printed shape resulting in lower

Fig. 37. REINFORCED_2 T-joint.

stiffness of the joint as only the top part of the bottom tube deforms in bending.

Fig. 36 shows the deformed shape of the two joints at the last iteration of the numerical simulations and after the experimental tests. The strain concentration happens at similar locations, being the main difference occurring between the deformed shapes. CB1 presents deformations on the lower horizontal struts of the bottom tube due to the large openings in the side walls. The experimental deformed shape of CB1 shows that the initial defects caused cracks, preventing the bottom tube from bending as a whole.

Fig. 38 compares the REINFORCED T-joints (REINFORCED1 and REINFORCED2) and the reference T-joints both in terms of the experimental test results and the numerical simulations. The REINFORCED_2 T-joint is exactly like REINFORCED_1 except for a reinforcement in the areas of the circular holes on the top part, as was also done for TUBE. Therefore, the optimized regions were identical (see Fig. 37).

In this case, there is an excellent match between all joints (experimental and numerical) in terms of initial stiffness (Table 7 and Fig. 38). Table 7 shows that the plastic resistance is significantly increased by approximately 30 % when comparing REINFORCED_1 and TUBE, and 40 % for REINFORCED_2 versus TUBE, at a load level well beyond 150 kN. The difference between REINFORCED_1 and REINFORCED_2 is explained by early yielding around the first bolt row and failure region. The average strain in the expected failure region (Point 2, Fig. 39) is about twice the average strain in the first bolt row (Point 1, Fig. 39) for the REINFORCED_2 specimen. However, for REINFORCED_1, the average strain in Point 2 is only 25 % higher than the average strain in Point 1. Analyzing the load at 5 % equivalent plastic strain, the same trends are observed as for the plastic resistance.

Figure 39shows that the REINFORCED_1 joint exhibited net cross-section failure at the first hole in the top part, outside the region of interest, while REINFORCED_2 failed by transverse tensile cracking in the top face of the bottom tube next to the diagonal legs connecting to the

Table 7
Properties of T-joints.

Name	Initial Stiffness	Plastic resistance	Ultimate Load	Volume	Volume DB	PRV ratio
	[kN/mm]	[kN]	[kN]	[mm3 x 10^3]	[mm3 x 10^3]	-
FEM_TUBE	100.78	145.92	-	410.4	155.36	0.81
EXP_TUBE_1	101.71	137.82	256.05	392.6	137.56	0.80
EXP_TUBE_2	105.50	150.89	273.16	402.2	133.42	0.86
FEM_CB1	102.62	151.68	-	418.7	163.66	0.83
EXP_CB1_1	62.42	127.51	204.99	467.0	211.96	0.62
EXP_CB1_2	74.86	134.84	210.49	474.7	205.92	0.65
FEM_REINFORCED_1	95.26	192.93	-	418.9	153.86	1.05
EXP_REINFORCED_1	105.33	177.82	276.69	389.1	134.06	1.04
FEM_REINFORCED_2	103.47	198.38	-	428.5	153.86	1.06
EXP_REINFORCED_2	108.30	207.73	313.62	419.1	114.46	1.13

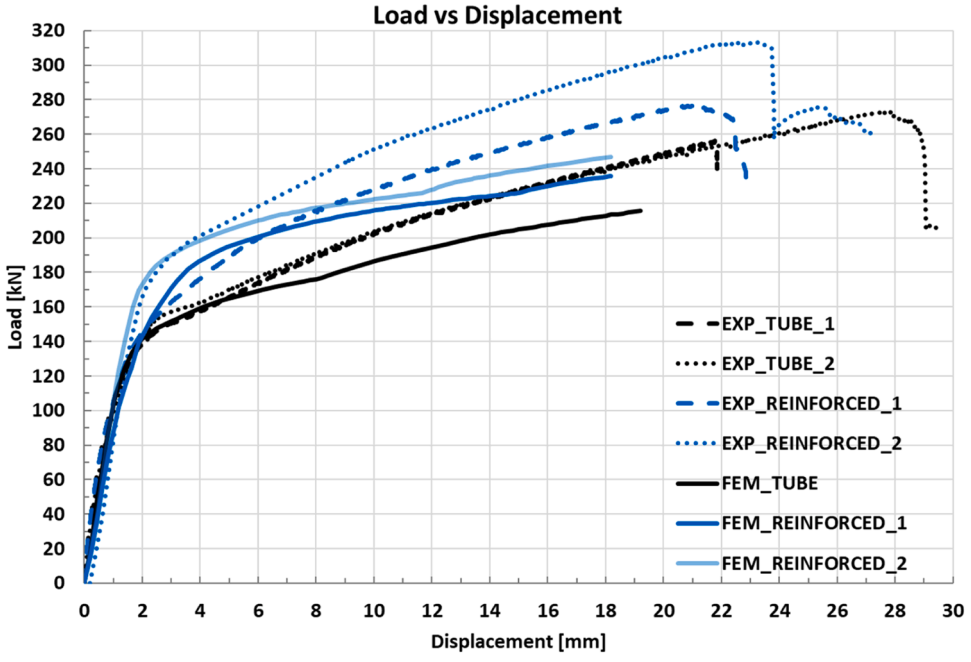

Fig. 38. TUBE (Non-optimized) vs. REINFORCED T-joints – Load vs Displacement curves.

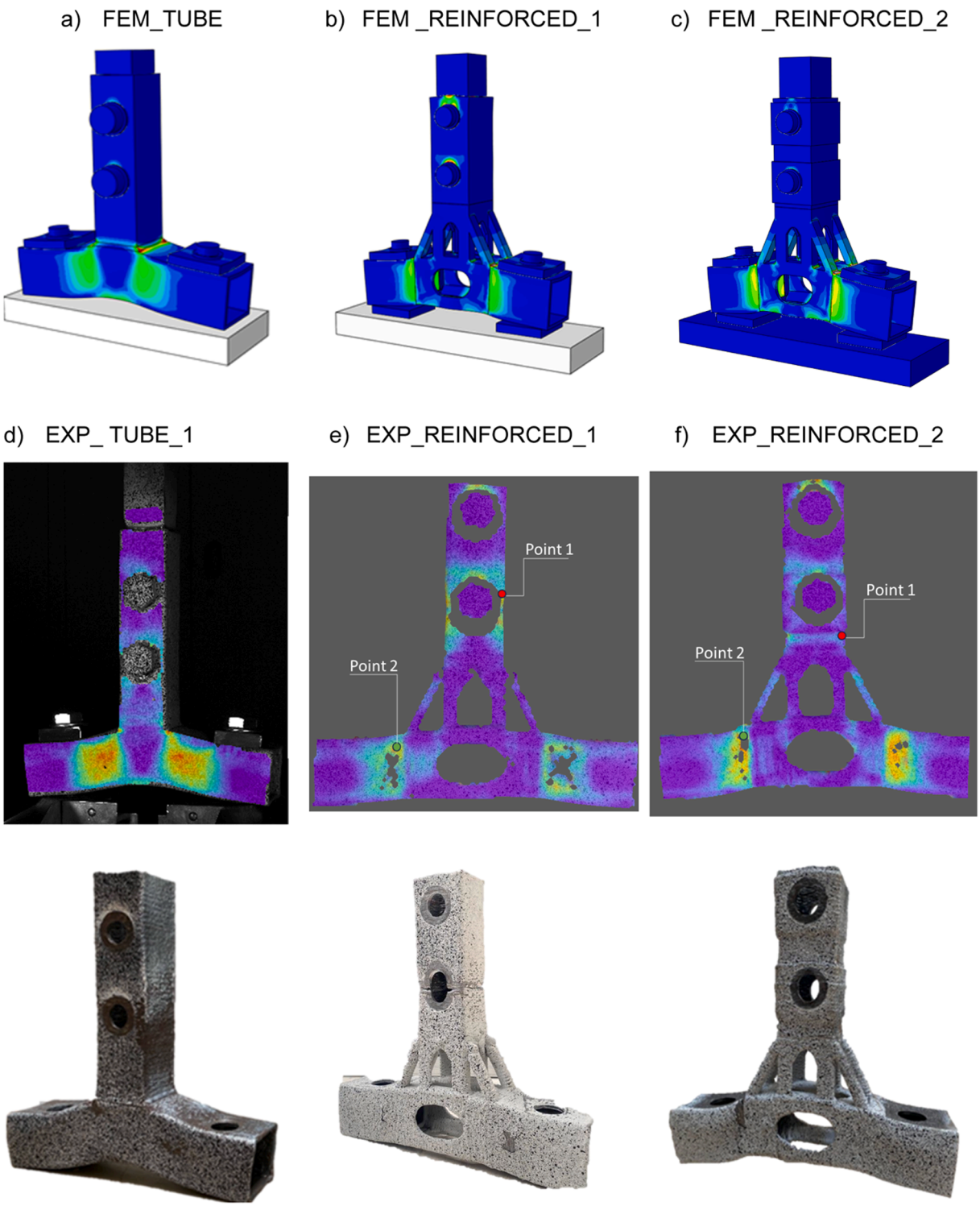

Fig. 39. Non-optimized (TUBE) vs. REINFORCED T-joints – Deformed shapes.

top tube. Finally, Fig. 40 and Table 7 shows that the REINFORCED joints used a similar amount of material with a better plastic resistance and ultimate load than the TUBE_1, which is the reference case in Fig. 40. As the volume of the experimental specimens has a small variation due to thickness variations and surface smoothness, a plastic resistance to volume ratio (PRV ratio) is introduced to see clearly the advantage of the REINFORCED T-joints. This ratio was calculated by dividing the normalized plastic resistance by the normalized volume (each one was normalized by the highest value of its column – highlighted in red on Table 7). To complement this information, the volume of the optimization region (Volume DB) alone is computed, which shows that the volume of the REINFORCED T-joints in that region of interests is smaller than the others.

8. Conclusions

This paper addressed the integration of topology optimization with wire arc additive manufactured steel based on a simple example of a T-

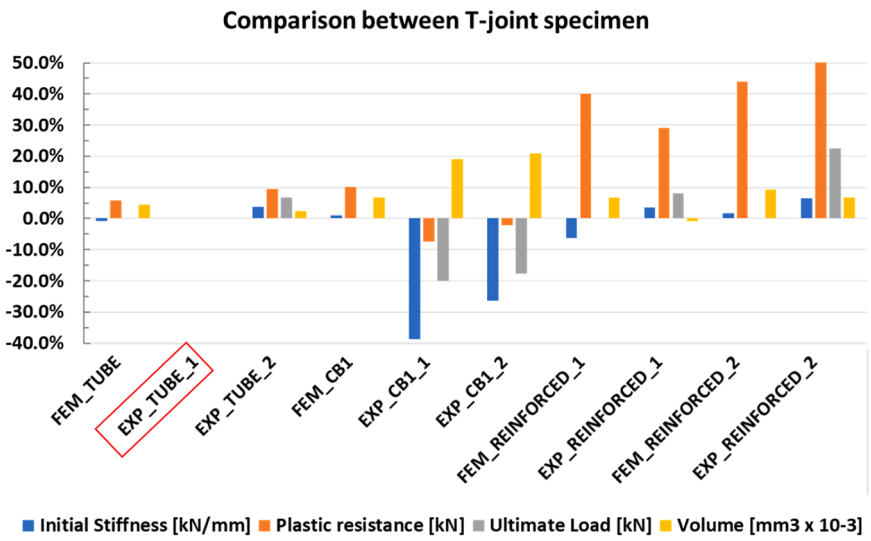

Fig. 40. Comparative assessment of the different cases.

joint. The complete workflow, from design to manufacture was considered. The following conclusions were achieved from this case study:

- Using a classical linear workflow that splits the CAD model (design and optimization), slicing and production are not compatible with practical applications because there is lack of guidance on how to perform TO, WAAM process limitations and preparation for manufacturing.
- The available optimization algorithms in structural analysis software led to significantly different optimized geometries. This confirms the need for guidance on how to apply TO in order to avoid iterations.- An iterative coupled workflow based on a digital process that takes advantage of interoperability between software can combine the mechanical criteria with the execution constraints and path planning.
- It was always necessary to assess the results of the optimization with advanced nonlinear material and geometrical FE analyses with imperfections to validate adequate structural performance.
- It was possible to overcome several challenges in the production step, namely related to the transition between the standard parts and the optimized parts, the printing of thinner parts, the execution of overhangs, and the achievement of smooth surfaces in the openings. A RE-ENGINEERING step was therefore proposed and validated.
- The best optimization of the T-joint (REINFORCED) was accomplished from a combination of two optimization results using different optimization regions, followed by a re-engineering step that reduces its volume and prepared the geometry for printing without impacting its properties.
- The T-joint case study was shown that an optimized solution can be designed and manufactured. It was proven by experimental tests that it is possible to achieve a gain of 30–35 % in plastic resistance with approximately the same amount of material.

While this study contributes valuable insights into all the steps of process and demonstrates the feasibility of an optimized geometry manufactured with WAAM, the process demands a finer structure. One avenue for future research is to construct a more 'linear' framework that includes all procedures (from first design to manufactured geometry) and each step can incorporate specifications from the others, which may lead to a more efficient and less iterative process. Moreover, a more comprehensive understanding of the integration of WAAM and TO may be obtained by applying this workflow to a different and more complex geometry. This gradual increment on the difficulty of the case study will lead to a feasible application in practical engineering problems.

CRediT authorship contribution statement

Santos Ana Francisca: Writing – review & editing, Validation. **Simões da Silva Luis:** Writing – review & editing, Validation, Supervision. **Tankova Trayana:** Writing – review & editing, Writing – original draft, Validation, Supervision, Methodology. **Zhu Carlos:** Writing – review & editing, Writing – original draft, Investigation. **Pinto Monteiro Kaike:** Writing – review & editing, Writing – original draft, Methodology, Investigation.

Declaration of Competing Interest

The authors declare that they have no known competing financial interests or personal relationships that could have appeared to influence the work reported in this paper.

Acknowledgements

This work was partly financed by:

i. FCT / MCTES through national funds (PIDDAC) under the R&D Unit Institute for Sustainability and Innovation in Structural Engineering (ISISE), under reference UIDB / 04029/2020, and under the Associate Laboratory Advanced Production and Intelligent Systems (ARISE) under reference LA/P/0112/2020.
ii. The doctoral grant 2022.11969.BD by the Portuguese Foundation for Science and Technology (FCT) attributed to the first author.
iii. The doctoral grant 2021.05992.BD by the Portuguese Foundation for Science and Technology (FCT) attributed to the second author.

References

[1] Bock T. The future of construction automation: technological disruption and the upcoming ubiquity of robotics. Autom Constr 2015;59:113–21. https://doi.org/10.1016/j.autcon.2015.07.022.
[2] Gardan N, Schneider A. Topological optimization of internal patterns and support in additive manufacturing. J Manuf Syst 2015;37:417–25. https://doi.org/10.1016/j.jmsy.2014.07.003.
[3] Zhu J, Zhou H, Wang C, Zhou L, Yuan S, Zhang W. A review of topology optimization for additive manufacturing: status and challenges. Chin J Aeronaut 2021;34:91–110. https://doi.org/10.1016/j.cja.2020.09.020.
[4] Harzheim L, Graf G. A review of optimization of cast parts using topology optimization: I - Topology optimization without manufacturing constraints. Struct Multidisc Optim 2005;30:491–7. https://doi.org/10.1007/s00158-005-0553-x.

[5] Wang C, Xu B, Meng Q, Rong J, Zhao Y. Topology optimization of cast parts considering parting surface position. Adv Eng Softw 2020;149:102886. https://doi.org/10.1016/j.advengsoft.2020.102886.
[6] Li T, Wang L. Bending behavior of sandwich composite structures with tunable 3D-printed core materials. Compos Struct 2017;175:46–57. https://doi.org/10.1016/j.compstruct.2017.05.001.
[7] Christensen PW, Klarbring A. An introduction to structural optimization. Dordrecht London: Springer; 2009.
[8] Mei L, Wang Q. Structural optimization in civil engineering: a literature review. Buildings 2021;11:66. https://doi.org/10.3390/buildings11020066.
[9] Wang D, Guan D, Zhu S, Kinnon MM, Geng G, Zhang Q, Zheng H, Lei T, Shao S, Gong P, Davis SJ. Economic footprint of California wildfires in 2018. Nat Sustain 2021;4:252–60. https://doi.org/10.1038/s41893-020-00646-7.
[10] Bendsoe MP, Sigmund O. Material interpolation schemes in topology optimization. Arch Appl Mech (Ing Arch) 1999;69:635–54. https://doi.org/10.1007/s004190050248.
[11] Zhang W, Zhu J, Gao T. Topology optimization in engineering structure design. London: iste Press; 2016.
[12] Sethian JA. Level set methods and fast marching methods: evolving interfaces in computational geometry, fluid mechanics, computer vision, and materials sciences. , [Nachdr.]. 2. ed. Cambridge: Cambridge Univ. Press; 2010.
[13] Allaire G, Jouve F, Toader A-M. A level-set method for shape optimization. Comptes Rendus Math 2002;334:1125–30. https://doi.org/10.1016/S1631-073X(02)02412-3.
[14] Wang MY, Wang X, Guo D. A level set method for structural topology optimization. Comput Methods Appl Mech Eng 2003;192:227–46. https://doi.org/10.1016/S0045-7825(02)00559-5.
[15] Young V, Querin OM, Steven GP, Xie YM. 3D and multiple load case bi-directional evolutionary structural optimization (BESO). Struct Optim 1999;18:183–92. https://doi.org/10.1007/BF01195993.
[16] Y.M. Xie, G.P. Steven, Evolutionary structural optimization, 1997. ⟨https://link.springer.com/book/10.1007/978-1-4471-0985-3⟩.
[17] Huang X, Xie YM. Evolutionary topology optimization of continuum structures: methods and applications. Chichester, UK: John Wiley & Sons, Ltd; 2010. https://doi.org/10.1002/9780470689486.
[18] Bendsoe MP, Sigmund O. Topology optimization: theory, methods and applications, nouv. ed. révisée et augm. Berlin: Springer; 2003.
[19] Bakhtiary N, Allinger P, Friedrich M, Mulfinger F. A new approach for sizing, shape and topology optimization. In: A new approach for sizing, shape and topology optimization. Detroid: SAE International; 1996. ⟨https://www.sae.org/content/960814/⟩.
[20] Wang C, Zhao Z, Zhou M, Sigmund O, Zhang XS. A comprehensive review of educational articles on structural and multidisciplinary optimization. Struct Multidisc Optim 2021;64:2827–80. https://doi.org/10.1007/s00158-021-03050-7.
[21] ABAQUS/Standard, 2023. ⟨https://www.3ds.com/products-services/simulia/products/abaqus/⟩ (Accessed August 7, 2023).
[22] Seifi H, Rezaee Javan A, Xu S, Zhao Y, Xie YM. Design optimization and additive manufacturing of nodes in gridshell structures. Eng Struct 2018;160:161–70. https://doi.org/10.1016/j.engstruct.2018.01.036.
[23] J. Chun, J. Lee, D. Park, TOPO-JOINT - Topology Optimization Framework for 3D-Printed Building Joints, in: Beijing, China, 2018: pp. 205–214. https://doi.org/10.52842/conf.caadria.2018.1.205.
[24] Hou J, Gu X, Zhu J, Wang J, Zhang W. Topology optimization of joint load control with geometrical nonlinearity. Chin J Aeronaut 2020;33:372–82. https://doi.org/10.1016/j.cja.2019.01.024.
[25] MX3D, MX3D Robot Arm, n.d. ⟨https://mx3d.com/industries/manufacturing/mx3d-robot-arm/⟩.
[26] MX3D, CONNECTOR FOR TAKENAKA, n.d. ⟨https://mx3d.com/industries/construction/connector-for-takenaka/⟩.
[27] Chen Y, Lu J, Wei Y. Topology optimization for manufacturability based on the visibility map. Comput-Aided Des Appl 2016;13:86–94. https://doi.org/10.1080/16864360.2015.1059199.
[28] Vatanabe SL, Lippi TN, de Lima CR, Paulino GH, Silva ECN. Topology optimization with manufacturing constraints: a unified projection-based approach. Adv Eng Softw 2016;100:97–112. https://doi.org/10.1016/j.advengsoft.2016.07.002.
[29] Liu J, Ma Y. A survey of manufacturing oriented topology optimization methods. Adv Eng Softw 2016;100:161–75. https://doi.org/10.1016/j.advengsoft.2016.07.017.
[30] Liu J, Gaynor AT, Chen S, Kang Z, Suresh K, Takezawa A, Li L, Kato J, Tang J, Wang CCL, Cheng L, Liang X, To AlbertC. Current and future trends in topology optimization for additive manufacturing. Struct Multidiscip Optim 2018;57:2457–83. https://doi.org/10.1007/s00158-018-1994-3.
[31] S. Galjaard, S. Hofman, N. Perry, S. Ren, Optimizing structural building elements in metal by using additive manufacturing, in: Proceedings of the International Association of Shell and Spacial Structures (IASS), Amsterdam, 2015.
[32] EOS, Additive Manufacturing for the new A350 XWB A350 XWB cable routing – from design to component in two weeks, n.d. ⟨https://www.eos.info/en/all-3d-printing-applications/airbus-a350-xwb-3d-printed-cable-mount⟩.
[33] Barroqueiro B, Andrade-Campos A, Valente RAF, Neto V. Metal additive manufacturing cycle in aerospace industry: a comprehensive review. JMMP 2019;3:52. https://doi.org/10.3390/jmmp3030052.
[34] Cooper K, Steele P, Cheng B, Chou K. Contact-free support structures for part overhangs in powder-bed metal additive manufacturing. Inventions 2017;3:2. https://doi.org/10.3390/inventions3010002.
[35] K. Vartanian, L. Brewer, K. Manley, T. Cobbs, Powder Bed Fusion vs. Directed Energy Deposition Benchmark Study: Mid-size Part with Simple Geometry, 2016. ⟨https://optomec.com/wp-content/uploads/2018/06/PBF-vs-DED-STUDY_Final_PDF.pdf⟩.
[36] Williams S, Martina F, Wood D, Garcia Colomo A. A comparison framework to support the selection of the best additive manufacturing process for specific aerospace applications. Int J Rapid Manuf 2020;9:1. https://doi.org/10.1504/IJRAPIDM.2020.10019230.
[37] Lange J, Feucht T, Erven M. 3D printing with steel: additive manufacturing for connections and structures. Steel Constr 2020;13:144–53. https://doi.org/10.1002/stco.202000031.
[38] Laghi V, Palermo M, Bruggi M, Gasparini G, Trombetti T. Blended structural optimization for wire-and-arc additively manufactured beams. Prog Addit Manuf 2023;8:381–92. https://doi.org/10.1007/s40964-022-00335-1.
[39] Ye J, Kyvelou P, Gilardi F, Lu H, Gilbert M, Gardner L. An end-to-end framework for the additive manufacture of optimized tubular structures. IEEE Access 2021;9:165476–89. https://doi.org/10.1109/ACCESS.2021.3132797.
[40] Mishra V, Ayas C, Langelaar M, Van Keulen F. Simultaneous topology and deposition direction optimization for Wire and Arc Additive Manufacturing. Manuf Lett 2022;31:45–51. https://doi.org/10.1016/j.mfglet.2021.05.011.
[41] Selvi S, Vishvaksenan A, Rajasekar E. Cold metal transfer (CMT) technology - an overview. Def Technol 2018;14:28–44. https://doi.org/10.1016/j.dt.2017.08.002.
[42] Pires JN, Azar AS, Nogueira F, Zhu CY, Branco R, Tankova T. The role of robotics in additive manufacturing: review of the AM processes and introduction of an intelligent system. Ind Robot Int J Robot Res Appl 2022;49:311–31. https://doi.org/10.1108/IR-06-2021-0110.
[43] Abaqus, Abaqus Theory Manual, 2011.
[44] Tankova T, Andrade D, Branco R, Zhu C, Rodrigues D, Simões da Silva L. Characterization of robotized CMT-WAAM carbon steel. J Constr Steel Res 2022;199:107624. https://doi.org/10.1016/j.jcsr.2022.107624.
[45] Rhinoceros 3D, 2023. ⟨https://www.rhino3d.com/⟩ (Accessed August 7, 2023).